AT2019cmw: a highly luminous, cooling featureless TDE candidate from the disruption of a high mass star in an early-type galaxy

Jacob L. Wise [ORCID],[1]* Daniel A. Perley [ORCID],[1] Nikhil Sarin [ORCID],[2] Tatsuya Matsumoto [ORCID],[3,4,5] K-Ryan Hinds [ORCID],[1] Yuhan Yao [ORCID],[6,7] Jesper Sollerman [ORCID],[8] Steve Schulze [ORCID],[9] Aleksandra Bochenek [ORCID],[1] Michael W. Coughlin [ORCID],[10] Kishalay De [ORCID],[11] Richard Dekany [ORCID],[12] Sara Frederick [ORCID],[13] Christoffer Fremling [ORCID],[12,14] Suvi Gezari [ORCID],[15,16] Matthew J. Graham [ORCID],[17] Anna Y. Q. Ho [ORCID],[18] Shrinivas Kulkarni [ORCID],[17] Russ R. Laher [ORCID],[19] Conor Omand [ORCID],[1] Natalya Johnson [ORCID],[20] Yashvi Sharma [ORCID],[17] Kirsty Taggart [ORCID],[21] Charlotte Ward [ORCID],[22] Avery Wold [ORCID][19] and Lin Yan [ORCID][12]

Affiliations are listed at the end of the paper

ABSTRACT

We present optical/UV photometric and spectroscopic observations, as well as X-ray and radio follow-up, of the extraordinary event AT2019cmw. With a peak bolometric luminosity of $\sim 10^{45.6}$ erg s^{-1}, it is one of the most luminous thermal transients ever discovered. Extensive spectroscopic follow-up post-peak showed only a featureless continuum throughout its evolution. This, combined with its nuclear location, blue colour at peak and lack of prior evidence of an AGN in its host lead us to interpret this event as a 'featureless' tidal disruption event (TDE). It displays photometric evolution atypical of most TDEs, cooling from ~ 30 to ~ 10 kK in the first ~ 300 d post-peak, with potential implications for future photometric selection of candidate TDEs. No X-ray or radio emission is detected, placing constraints on the presence of on-axis jetted emission or a visible inner-accretion disc. Modelling the optical light curve with existing theoretical prescriptions, we find that AT2019cmw may be the result of the disruption of a star in the tens of solar masses by a supermassive black hole (SMBH). Combined with a lack of detectable star formation in its host galaxy, it could imply the existence of a localized region of star formation around the SMBH. This could provide a new window to probe nuclear star formation and the shape of the initial mass function (IMF) in close proximity to SMBHs out to relatively high redshifts.

Key words: methods: observational – supernovae: individual: AT2019cmw – transients: tidal disruption events.

1 INTRODUCTION

In recent years, wide-area sky surveys have enabled the discovery of thousands of astronomical transients. Current on sky facilities include the Zwicky Transient Facility (ZTF; E. Bellm & S. Kulkarni 2017; E. C. Bellm et al. 2019; M. J. Graham et al. 2019; F. J. Masci et al. 2019; R. Dekany et al. 2020), the Gravitational-wave Optical Transient Observer (GOTO; D. Steeghs et al. 2022), the Asteroid Terrestrial Last Alert System (ATLAS; J. L. Tonry et al. 2018; K. W. Smith et al. 2020), the All-Sky Automated Survey for Supernovae (ASAS–SN; B. J. Shappee et al. 2014; C. S. Kochanek et al. 2017; K. Hart et al. 2023), the Catalina Sky Survey (CSS; S. Larson et al. 1998, 2003 and associated Catalina Real-time Transient Survey (CRTS; A. J. Drake et al. 2009; S. G. Djorgovski et al. 2011; A. A. Mahabal et al. 2011), and Pan-STARRS1 (PS1; K. C. Chambers et al. 2016; H. A. Flewelling et al. 2020). ZTF images the entire northern sky in both *g* and *r* filters on a ~ 48 h cadence down to an apparent magnitude of ~ 20.5 (E. Bellm &

S. Kulkarni 2017; E. C. Bellm et al. 2019), and includes a dedicated facility for spectroscopic follow-up (N. Blagorodnova et al. 2018; M. Rigault et al. 2019). This enables complete population-level studies of astrophysical transients, such as the Bright Transient Survey (BTS) – a large, purely magnitude-limited classification survey that has so far accumulated over 10 000 classified events. (C. Fremling et al. 2020; D. A. Perley et al. 2020; N. Rehemtulla et al. 2024).

In addition to classifying large numbers of supernovae (SNe) belonging to well-established types, ZTF has also discovered and characterized significant numbers of much rarer transients that may require energy sources or explosion mechanisms distinct from normal thermonuclear and core-collapse SNe. Examples include hydrogen-poor Type I Superluminous Supernovae (SLSNe; C. Inserra et al. 2018; A. Gal-Yam 2019) and Luminous Fast Blue Optical Transients (LFBOTs; M. R. Drout et al. 2014; R. Margutti et al. 2019; D. A. Perley et al. 2019; B. D. Metzger 2022a; A. Y. Q. Ho et al. 2023; A. A. Chrimes et al. 2024).

Similarly, an increasing number of tidal disruption events (TDEs), the flares produced when a star passes sufficiently close to a black hole to be torn apart and subsequently accreted (M.

J. Rees 1988; E. S. Phinney 1989), have been categorized. Observationally, TDEs have been discovered at a variety of electromagnetic wavelengths, including in the infrared (T. M. Reynolds et al. 2022; M. Masterson et al. 2024), UV/optical (S. Velzen et al. 2019, 2021; E. Hammerstein et al. 2023; Y. Yao et al. 2023), soft X-ray (S. Sazonov et al. 2021; I. Grotova et al. 2025; B. O'Connor et al. 2025), and hard X-ray (J. S. Bloom et al. 2011; Y. Yao et al. 2024; A. Y. Q. Ho et al. 2025). Candidate TDE neutrino associations have also been proposed (R. Stein et al. 2021; S. Reusch et al. 2022; N. Jiang et al. 2023; S. Velzen et al. 2024; C. Yuan, W. Winter & C. Lunardini 2024), suggesting the possibility for future multimessenger selection of TDEs. Additionally, other recently discovered classes of nuclear transients in galaxies have been proposed to be potentially caused by TDEs, such as 'ambiguous nuclear transients' (ANTs; B. Trakhtenbrot et al. 2019; S. R. Oates et al. 2024; P. Wiseman et al. 2025) and 'extreme nuclear transients' (ENTs; J. T. Hinkle et al. 2025), which appear spectrally similar to active galactic nuclei (AGNs).

Observationally, optically selected TDEs typically display a blackbody continuum with a characteristic temperature between 10^4-10^5 K, whilst also showing little temperature evolution post-peak. Additionally, the photospheres of these TDEs appear to decrease in radius over their evolution (S. Velzen et al. 2021; E. Hammerstein et al. 2023). Post-peak, their luminosities approximately follow a $t^{-5/3}$ power-law decay, consistent with the predicted rate of mass fallback from a tidally disrupted star (M. J. Rees 1988; E. S. Phinney 1989; S. Gezari 2021).

Whilst some of the optically selected TDEs in the samples from S. Velzen et al. (2021), E. Hammerstein et al. (2023), and Y. Yao et al. (2023) are X-ray bright in addition to displaying UV/optical emission, some do not produce detectable X-ray emission and yet are still optically bright. The exact physical source of this UV/optical emission in the absence of detected X-ray emission is a topic of debate, with several hypotheses proposed to explain these observations. These include energy liberated from collisions of in-falling stellar debris rather than accretion (S. S. Kim, M.-G. Park & H. M. Lee 1999), and reprocessing of X-ray emission from accretion by an extended optically thick outflow (E. J. Parkinson et al. 2022).

Sample studies of TDEs have recently begun to reveal subpopulations of TDEs with peculiar characteristics. For example, E. Hammerstein et al. (2023) found 4 events in their sample of 30 which are 2 to 4 times more luminous than any TDEs of other spectral classes in their sample, with $L_{peak} \geq 10^{45}$ erg s^{-1}. They also appear to display no broad UV/optical emission features, in contrast to most other TDEs previously seen. E. Hammerstein et al. (2023) proposed that they are part of a new distinct rare subclass of extreme 'featureless' TDEs. The majority of TDEs appear to show little temperature evolution post-peak (S. Velzen et al. 2021). However, a small number of events are characterized by significant post-peak reddening (Y. Yao et al. 2023), with a notable example being the candidate featureless TDE 'Dougie' (J. Vinkó et al. 2014). In the case of both featureless TDEs and those that display post-peak cooling, the physical mechanism that separates them from 'regular' TDEs is currently unknown. Understanding these mechanisms and how these TDEs evolve would be beneficial for sample studies of both SLSNe and TDEs, as some SLSNe can also appear spectroscopically featureless at early times, and all appear to cool post-peak.

Studies of TDEs at top of the observed luminosity distribution have also begun to find an increasing number of disrupted stars with potentially high masses. In terms of the masses of disrupted

stars in TDEs, most events from sample studies such as E. Hammerstein et al. (2023) are estimated to have masses on the order of $\sim 1 M_\odot$ or less. As stated by B. Mockler, J. Guillochon & E. Ramirez-Ruiz (2019), this is expected due to the stellar Initial Mass Function (IMF) being bottom heavy. However, as the number of TDEs discovered by ongoing sky surveys has grown a small number of events have been discovered that have been hypothesized to be from the disruption of high mass stars ($\gtrsim 10 M_\odot$), such as AT2021lwx (B. M. Subrayan et al. 2023; J. T. Hinkle et al. 2025) and AT2023vto (H. Kumar et al. 2024). Whilst these types of events are intrinsically rare, their higher luminosity than TDEs of lower mass stars mean that they are observable out to higher redshifts.

In this paper, we present a comprehensive analysis of AT2019cmw, first categorized by Y. Yao et al. (2023) as a member of the 'TDE-featureless' class (E. Hammerstein et al. 2023). It was noted as a prominent outlier in the BTS by D. A. Perley et al. (2020). At a redshift of $z = 0.519$, it was the most luminous event seen in the survey by a significant margin. Due to its extreme luminosity and peculiar spectral appearance, it had no analogous events in the BTS, although it is somewhat observationally similar to ASASSN-15lh (S. Dong et al. 2016; G. Leloudas et al. 2016; A. Mummery & S. A. Balbus 2020) and Dougie (J. Vinkó et al. 2014).

Our extensive follow-up campaign is detailed in Section 2, with blackbody characteristics derived from multiwavelength photometry summarized in Section 3.2. We go on to discuss a variety of possible physical interpretations in Section 4. In order to constrain other characteristics of the system such as the mass of the disrupted star, we also model the transient using the 'cooling envelope' TDE model fit using the Bayesian inference transient modelling software REDBACK, detailed in Sections 5.1 and 5.3. We also consider an alternate 'reprocessing-outflow' model in Section 6. Discussion of our findings is detailed in Section 7. Our conclusions are summarized in Section 8.

We assume a Flat Lambda-CDM cosmology with $\Omega_m = 0.3111$, $\Omega_\Lambda = 0.6889$ and $h = 0.6766$ (N. Aghanim et al. 2020). Optical and UV magnitudes are in the AB system, and uncertainties are quoted at the 1σ level unless otherwise specified.

2 OBSERVATIONS

AT2019cmw was first reported to the Transient Name Server (TNS) on MJD 58567.51 by the ZTF collaboration at an r-band magnitude of 19.33 (J. Nordin et al. 2019). The transient rose to peak approximately 20 to 30 d after the initial alert from ZTF. Initially flagged as an SLSN candidate due to its blue colour, slow evolution and faint host, a multi-observatory photometric and spectroscopic follow-up campaign was undertaken over the following months. Interest in AT2019cmw was further spurred when spectroscopic observations, as detailed in Section 2.5, revealed it to have a notably high redshift and thus luminosity.

2.1 ZTF and ATLAS forced photometry

Forced photometry was carried out using the ZTF forced-photometry service (F. J. Masci et al. 2019) via the ZTF FRITZ marshal, an instance of SKYPORTAL (S. Walt, A. Crellin-Quick & J. Bloom 2019; M. W. Coughlin et al. 2023), from MJD 58198.42 onwards. Data points with a SNR < 3 were discarded, as well as 41 exposures from field number 1801 due to the reference image for this field being contaminated with flux from the transient. The earliest 3σ forced photometry detection was at MJD 58558.47 in

g-band, 9.03 d earlier than the first ZTF alert was reported to TNS, and the last detection was at MJD 59056.34 in *r*band. Outside of these dates, we find upper limits of $\gtrsim 21$ mag throughout.

Forced photometry was also carried out using the ATLAS forced photometry web service (J. L. Tonry et al. 2018; K. W. Smith et al. 2020; L. Shingles et al. 2021) from MJD 57233.35 onwards. The transient's first 3σ detection was at MJD 58594.61 and the last detection was at MJD 58788.26 in *o* -band, with upper-limits of $\gtrsim 20$ outside of these dates. All datapoints that passed the SNR cut were used, except for one ATLAS *o*-band data point at MJD 58810.19. This detection was ~ 2 mag brighter than previous ATLAS forced photometry detections, as well as ZTF *r*-band and LT *r* band detections at similar epochs, and so was considered an outlier and discarded. Reference images used in the image subtraction were updated on MJD 58 417 and MJD 58882, before the first significant detection for the former and after the last significant detection for the latter, and so flux contamination from the transient was not an issue.

2.2 Liverpool telescope

AT2019cmw was observed with the Liverpool Telescope (LT) IO:O imager in the Sloan Digital Sky Survey (SDSS) filters *griz* starting at MJD 58594.14, shortly after the light-curve's peak in ZTF, with *u*-band observations included from MJD 58603.10. *u*-band observations continued until MJD 58779.86, and *z*-band continued until MJD 58779.87, after which the transient was too faint in these bands. *gri* observations continued until MJD 59041.99. All images were reduced using the LT automatic data reduction pipeline.

ugriz images taken on the same night were stacked using SWARP (E. Bertin et al. 2002). Image subtraction and point source function (PSF) photometry was then performed on *griz* images using SUBPHOT_PIPE[1]. Their pipeline uses Point Spread Function Extractor (PSFEx; E. Bertin 2013) to cross-convolve the PSF from the science image and a PS1 reference image, with the convolved PSF then fit to the science and reference images to measure each respective image. This PSF-fitting method is based on the method from A. Gal-Yam et al. (2008) and C. Fremling et al. (2016). Image subtraction was then performed using the reference images from the PS1 survey. The magnitudes of comparison stars in the image used to calculate the zeropoint, as well as the magnitude of the transient, were found by measuring fluxes using the extracted PSFs applied to subtracted images.

u-band photometry was extracted using relative aperture photometry of the transient and foreground comparison stars in the images, using the PYTHON implementation of SOURCE EXTRACTOR (E. Bertin & S. Arnouts 1996) SEP (K. Barbary 2016). As the host is red in PS1 with a *g*-band magnitude of > 22 (see Fig. 1 and Section 3.4), we assume that any host contamination within the aperture in *u*-band is negligible compared with the transient flux, and can be ignored. As a result, we do not perform image subtraction for our *u*-band images. The zeropoint of a chosen reference exposure of the transient's field was found using exposures of the LT photometric standard SA114-654 taken on the same photometric night of 2019-09-01. Two observations of the standard at varying airmasses during the night were used to find the *u*-band atmospheric extinction coefficient, and the above-atmosphere filter zeropoint for the night. This zeropoint
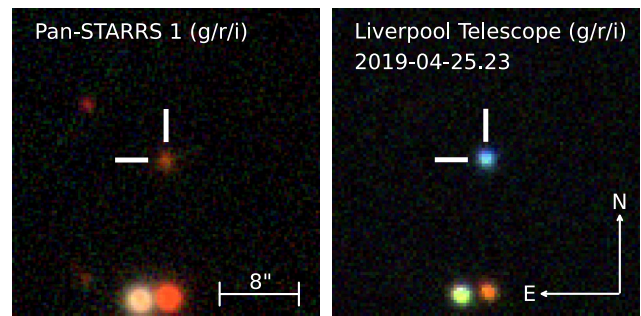
[1] https://github.com/kryanhinds/subphot_pipe

Figure 1. **Left:** PS1 *gri* composite image of AT2019cmw's host. **Right:** LT IO:O *gri* composite image taken ~ 4.8 d post-peak in AT2019cmw's rest-frame.

was used to calculate the above-atmosphere magnitudes of foreground stars in the field, which were then used to find the zeropoints of all epochs. After conducting a median background subtraction, photometry of AT2019cmw was performed using a 1.75 arcmin radius aperture.

We also present supplementary LT *griz* photometry for the featureless TDE AT2018jbv from E. Hammerstein et al. (2023), which will be discussed in Sections 5 and 7.3, taken between MJD 58547.047 and MJD 59024.934. This photometry was reduced using the same method of image subtraction and PSF photometry as detailed above for AT2019cmw's *griz* photometry. We list LT photometry for AT2018jbv in Table A2.

2.3 *Swift*

Ten epochs of observations were taken using the Neil Gehrels *Swift* Observatory (N. Gehrels et al. 2004), Ultraviolet Optical Telescope (UVOT; P. W. A. Roming et al. 2005) and X-Ray Telescope (XRT; D. N. Burrows et al. 2005) from MJD 58608.48 to MJD 58673.28.

We used the UVOTSOURCE package as part of the HEASOFT software bundle to reduce *UVOT* images, which utilises FTOOLS (J. K. Blackburn et al. 1999) to extract magnitudes. A 5 arcmin radius aperture was chosen to maximise the flux from the transient in order to achieve an optimal SNR. Six circular regions surrounding the target that contained few or no visible sources with radii ranging from 8 to 32 arcmin were chosen to compute the background. As was the case for LT IO:O *u*-band photometry as described in Section 2.2, host contamination within the aperture can be considered to be negligible, and so no image subtraction was performed. Photometry from the UVOT *U*, *B*, and *V* bands was excluded due to poor SNR. Our first and last significant detections were at MJD 58608.54 and MJD 58642.20, respectively, both in *UVW*1.

ZTF, ATLAS, LT and *Swift* lightcurves are shown in Fig. 2.

XRT observations were taken simultaneously with *UVOT* observations for a total of 14.94 ks. A stack of all 10 epochs yielded a non-detection with a 3σ count-rate upper limit of $< 5.355 \times 10^{-4}$ ct s^{-1} at the transient's position. Assuming a spectral shape of a power law with a photon index of 2, and with a Galactic neutral hydrogen column density of 4.33×10^{20}cm^{-2} (HI4PI Collaboration 2016) whilst ignoring any absorption, this corresponds to an absorbed flux upper limit of $< 1.883 \times 10^{-14}$ erg s^{-1}cm^{-2} between 0.3–10 keV.
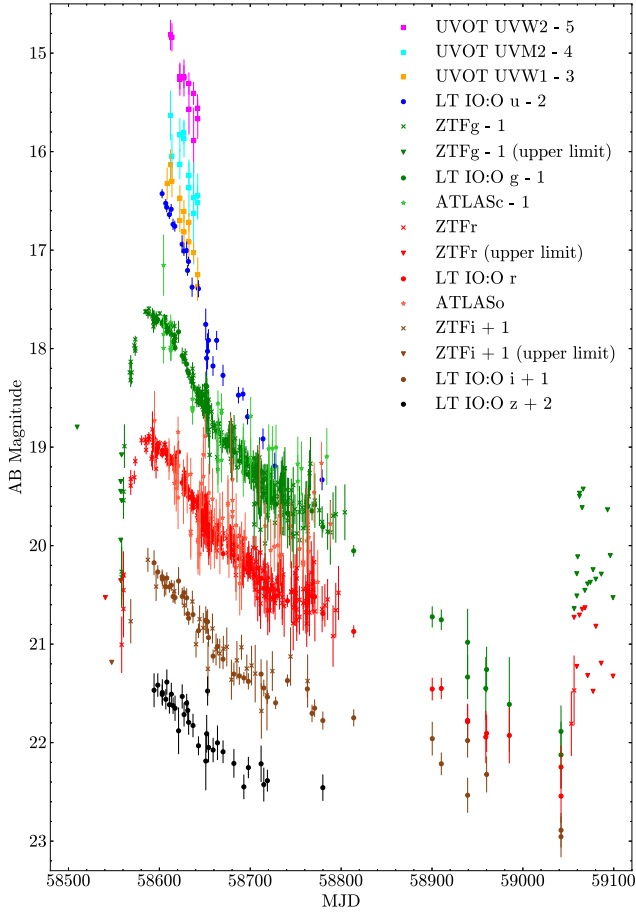
Figure 2. A combined plot of *ugriz* photometry from LT IO:O, ZTF *gri* forced photometry, ATLAS *co* forced photometry, and *uvw*1, *uvm*2 , and *uvw*2 UVOT photometry from *Swift*. An offset has been applied to all photometric bands except r in order to show each band separately. ZTF and LT *gri* photometry, as well as ATLAS *co* photometry has been overlaid. ZTF forced photometry 3σ upper limits have also been plotted up to 50 d before and after the first and last significant forced photometry detections respectively.

2.4 NEOWISE

Photometry was obtained using the NASA IRSA online catalogue from the Near-Earth Object Wide-field Infrared Survey Explorer (NEOWISE) Reactivation Mission (A. Mainzer et al. 2014), an infrared sky survey mission using the 3.4 μm (W1) and 4.6 μm (W2) filters from the *Wide-Field Infrared Explorer* (*WISE*; E. L. Wright et al. 2010). Using IRSA, a search was performed at the target's location within a circular region with 2.5 arcmin radius, with the resulting photometry then binned over intervals of 100 d. For the filter W1 only detections with a SNR > 2 were used, and for W2 all detections were used as detections in this filter were more marginal. An error weighted average of these fluxes was then used to calculate the magnitudes for each 100-d bin.

Fig. 3 shows the NEOWISE photometry found using this method from MJD 56948.07 to MJD 59850.88 for AT2019cmw's host. To search for any IR variability from AT2019cmw's host during this time period that may be caused by the transient or a pre-existing AGN, we compare flux from individual epochs of NEOWISE photometry to the weighted averages of all epochs for both filters. Most epochs show no significant deviation from the
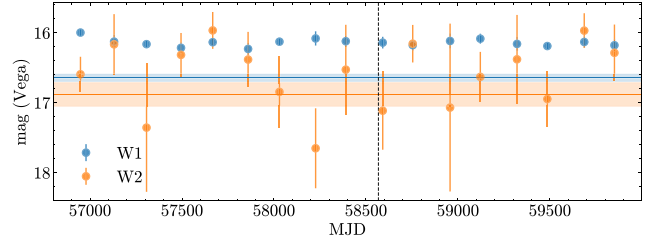

Figure 3. Vega-magnitude plot of NEOWISE W1 (blue) and W2 (orange) photometry at the location of AT2019cmw from MJD 56948.07 to MJD 59850.88, with AT2019cmw's earliest ZTF forced photometry detection at MJD 58558.47 marked by the black vertical dashed line. Datapoints show NEOWISE photometry values found using the method outlined in Section 2.4, with error bars corresponding to 1σ errors. Solid horizontal lines and shaded regions show ALLWISE W1 and W2 photometry values in the same colours.

weighted mean in each filter. The most significant deviation that we see is at MJD 56948.03, it is brighter than the weighted mean in W1 with a deviation of $\sim 2.6\sigma$, whereas in W2 it is fainter with a deviation of $\sim 0.8\sigma$. As a $\sim 2.6\sigma$ is expected ~ 1 per cent of the time for any particular measurement, there is a ~ 34 per cent chance of this occurring for a photometric data point over our observations. Also, this deviation did not occur in both filters simultaneously. We therefore do not consider the location of AT2019cmw to to have significantly variable IR flux during the time period in which it was observed.

By subtracting the average baseline flux pre-transient from the brightest detections at the location of AT2019cmw post-transient onset, at MJD 59121.73 for W1 and MJD 59686.59 for W2, we find upper-limits of W1 > 16.74 and W2 > 16.27.

We also plot ALLWISE photometry from MJD 55302.78 to MJD 55487.19 for comparison, which has magnitudes of $W1 = 16.64 \pm 0.05$ and $W2 = 16.88 \pm 0.17$ (Vega). The host was not significantly detected in $W3$ or $W4$. As can also be seen in Fig. 3, AT2019cmw's NEOWISE photometry in W1 is consistently significantly brighter than in ALLWISE at all observed epochs. However, we do not consider this discrepancy to be physical, as for faint objects such as AT2019cmw's host NEOWISE is known to overestimate flux in the W1 band compared to ALLWISE by up to half a magnitude[2].

2.5 Spectroscopy

Spectra were taken using the SED Machine (SEDM; N. Blagorodnova et al. 2018; M. Rigault et al. 2019) on the Palomar 60-inch telescope, the Double Spectrograph (DBSP; J. B. Oke & J. E. Gunn 1982) on the Palomar 200-inch telescope, the DeVeny Optical Spectrograph (T. A. Bida et al. 2014) on the 4.3 meter Lowell Discovery Telescope (LDT), and the Low Resolution Imaging Spectrometer (LRIS; J. B. Oke et al. 1995) on the 10 meter Keck I telescope. These spectra were reduced using the same methods detailed in appendix B of Y. Yao et al. (2022). Instrumental set-ups for each observation are detailed in Table 1.

As seen in Fig. 4, AT2019cmw remains spectroscopically featureless for its entire observed evolution in the optical, and displays none of the prominent broad emission features seen in most

---

[2]https://wise2.ipac.caltech.edu/docs/release/neowise/expsup/sec2_1c.html

Table 1. Spectroscopic set-ups for observations shown in Fig. 4.

MJD	Phase d, rest	Telescope/Instrument	Grating	Slit width '	Exposure s
58591.38	+22	P60/SEDM	IFU	N/A	2250
58597.49	+26	P200/DBSP	600/4000	1.5	600
58605.45	+31	LDT/DeVeny	300/4000	1.5	1200
58632.44	+49	LDT/DeVeny	300/4000	1.5	1600
58668.54	+72	Keck/LRIS	400/3400,400/8500	1	900 800
58696.28	+91	P200/DBSP	600/4000	1.5	900
58783.31	+148	Keck/LRIS	400/3400,400/8500	1	600 540
58930.61	+245	Keck/LRIS	400/3400,400/8500	1	900 900
59372.59	+536	Keck/LRIS	400/3400,400/8500	1	1200,1130

TDEs. For instance, the hydrogen, helium, oxygen and nitrogen emission features used to define the classification scheme from S. Velzen et al. (2021) are absent. Less common features such as Fe II, as seen in the case of AT2018fyk (T. Wevers et al. 2019), are also not present. At late times, spectra appear host-dominated.

As is also shown in Fig. 4, Mg II absorption from the intervening interstellar/intergalactic medium can be seen in the majority of our spectra. We also see the K, H , and G Fraunhofer lines of calcium in many of our spectra at the same redshift. Using these lines, we measure a redshift for AT2019cmw of $z = 0.519$. After applying a $2.5\log_{10}(1 + z)$ K-correction, this implies a peak rest-frame u-band magnitude of M $= -23.6$, as was also found by D. A. Perley et al. (2020).

2.6 VLA

The transient's location was observed with the Karl G. Jansky Very Large Array (VLA; A. R. Thompson et al. 1980; R. A. Perley et al. 2011) radio telescope as part of a late-time TDE follow-up programme (ID: 23A–280; Y. Yao et al. 2025). The observation of AT2019cmw started at MJD 60033.34, 1474.86 d after the first ZTF forced photometry detection. The total on-source integration time was 5.026 h in the VLA C-band (4–8 GHz), with array configuration B used. AT2019cmw was undetected down to a 3σ upper limit of 4.5 μJy. The data was analysed following the standard radio continuum image analysis procedures in the Common Astronomy Software Applications (CASA; T. C. Team 2022).

3 CHARACTERISTICS

In this section, we use the data described in Section 2 to infer physical properties of AT2019cmw.

3.1 Rise time to peak

In order to constrain the date of peak brightness, we fit curves to the first 100 d of g-band forced photometry using bootstrapped Locally Weighted Scatterplot Smoothing (LOWESS; W. S. Cleveland 1979, 1981), incorporating the INTERP1D function from SCIPY (P. Virtanen et al. 2020). The local regression was repeated using a range of fractions of the data from 0.07 to 0.17 in increments of 0.01, with each fit repeated 1000 times. From this, we estimate that the transient peak occurred on MJD $58590.9^{+2.3}_{-2.7}$ in observer-frame g-band, which we use in the analysis hereon. AT2019cmw thus has a rise time from first significant detection to peak brightness of $21.35^{+1.51}_{-1.78}$ d in its rest frame.

3.2 Pseudo-blackbody fits

We fit blackbody SEDs to AT2019cmw's ZTF, ATLAS, LT, and *Swift* photometry. Optical photometry of AT2019cmw was corrected for Galactic foreground extinction using $A_\lambda/E(B - V)$ values derived by E. F. Schlafly & D. P. Finkbeiner (2011), and *Swift* UVOT UV photometry was corrected using $A_\lambda/E(B - V)$ values from table 2 of A. D. Code et al. (1976). All photometry was corrected using $E(B - V) = 0.0438$ mag as measured by E. F. Schlafly & D. P. Finkbeiner (2011) at the location of the transient. Effective wavelengths for each observed filter were found using SVO filter profile service (C. Rodrigo, E. Solano & A. Bayo 2012; C. Rodrigo & E. Solano 2020). Photometry was then corrected for time dilation and redshift effects.

In order to determine the radius and temperature evolution of AT2019cmw, we then fit Planck function SEDs using the SCIPY CURVE_FIT function to our photometry in 1 d intervals. We only consider days with observations in more than 3 photometric bands, as we are simultaneously fitting two free parameters. The luminosity at each epoch was then found using $L = 4\pi R^2 \sigma T^4$.

1σ confidence intervals for AT2019cmw's blackbody characteristics were deduced using the bootstrapping method. Using the RESAMPLE function from SCIKIT-LEARN (L. Buitinck et al. 2013), the photometry and the uncertainties on each measurement were randomly resampled a large number of times (>1000) in order to produce a distribution of derived values of L, T , and R for each fitted epoch. The overall trends of its blackbody evolution were then found by interpolating its derived blackbody characteristics using bootstrapped LOWESS.

Due to poor photometric coverage, we were unable to constrain its pre-peak blackbody characteristics using the method outlined above. To obtain estimates of its blackbody evolution pre-peak, we make the assumption that AT2019cmw's cooling began at peak and fix its temperature to the peak value found by LOWESS interpolation of post-peak epochs as detailed above. An approximately steady blackbody temperature pre-peak has been previously observed in a variety of TDEs. For example, fig. 10 from T. W.-S. Holoien et al. (2019) shows this behaviour for the TDEs ASASSN-19bt and ASASSN-18pg (G. Leloudas et al. 2019; T. W.-S. Holoien et al. 2020). The featureless TDEs from E. Hammerstein et al. (2023), as can be seen in Fig. 5, also showed little temperature evolution pre-peak. Additionally, this has been shown to be the case for TDEs that cool post-peak. As can be seen in Supplementary fig. 2 from C. R. Angus et al. (2022), the cooling TDE AT2020neh did not appear to show significant temperature evolution until after peak luminosity, although its coverage is poor. We use this assumption, as AT2019cmw has previously been classified and analysed as a TDE by Y. Yao et al.
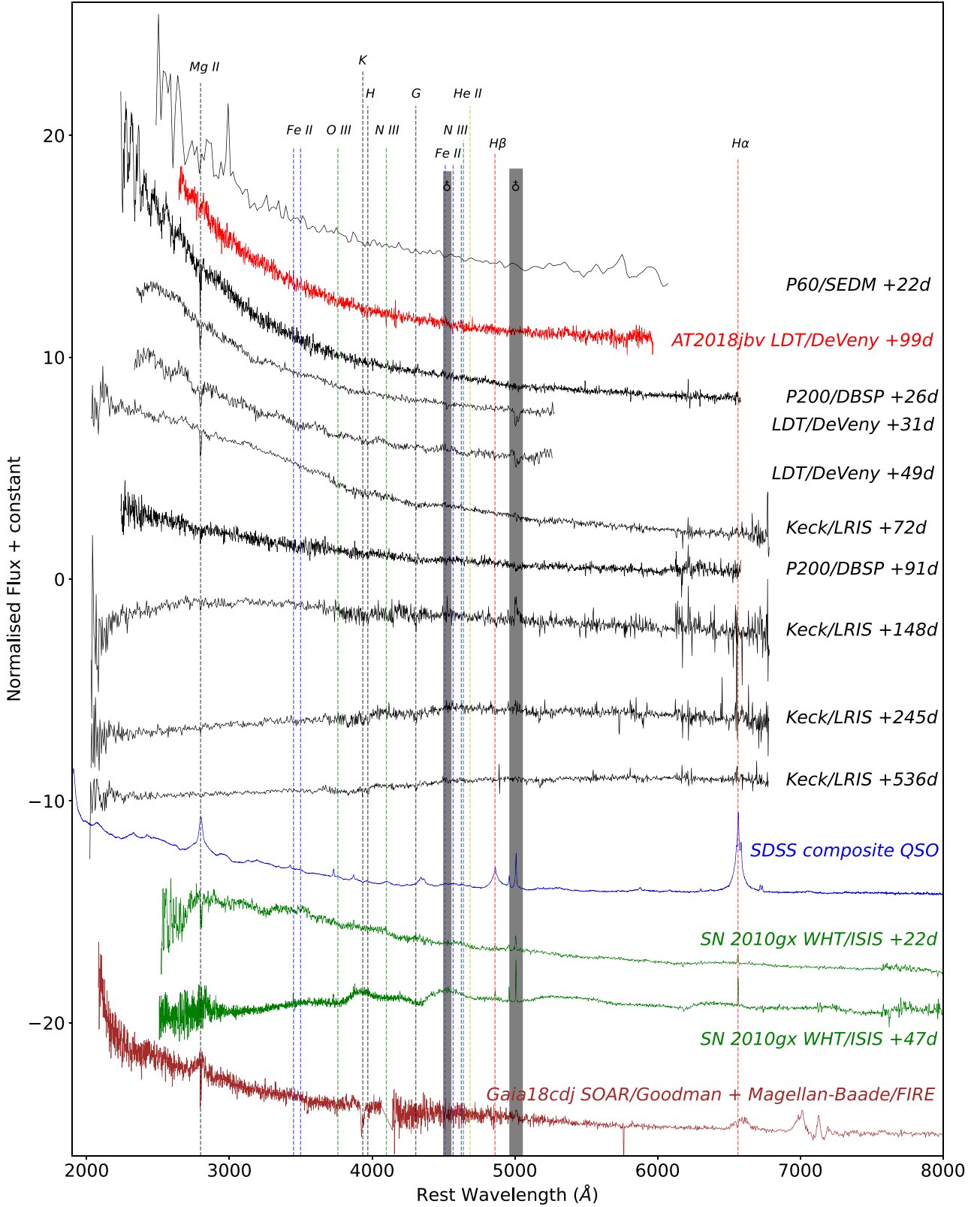
Figure 4. Spectra of AT2019cmw from Palomar P60, Palomar P200, LDT, and Keck LRIS in descending order of their observation, with time in days since first ZTF forced photometry detection in the AT2019cmw's rest frame. The positions of key spectral lines from the classification scheme outlined by S. Velzen et al. (2021) have been labelled. Mg II absorption and the K, H, and G Fraunhofer lines of calcium have also been labelled. Late-time LRIS spectra are host galaxy dominated. Also plotted for comparison are an LDT spectrum of the featureless TDE AT2018jbv (E. Hammerstein et al. 2023), an SDSS QSO composite spectrum (D. E. Vanden Berk et al. 2001) and two WHT ISIS spectra of the SLSN–I SN 2010gx (A. Pastorello et al. 2010). We also show a combined SOAR Goodman and Magellan–Baade FIRE spectrum of the ENT Gaia18cdj (J. T. Hinkle et al. 2025), taken ∼ 2 and ∼ 3.5 yr post-first detection in the transient's rest-frame respectively. Spectra have been normalized to their respective mean rest-frame flux between 4000 and 5000 Å.
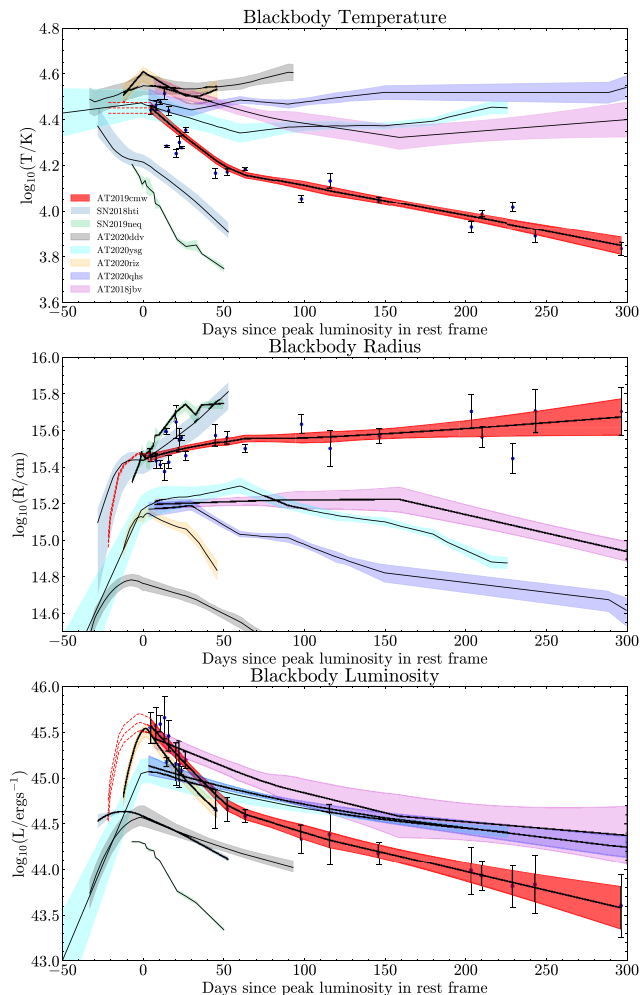
Figure 5. Pseudo-blackbody temperatures (**top**), radii (**middle**), and luminosities (**bottom**) of AT2019cmw and four featureless TDEs (AT2018jbv, AT2020riz, AT2020qhs, and AT2020ysg) from E. Hammerstein et al. (2023), with the most luminous TDE with spectral features from their sample (AT2020ddv, classified as TDE-He) also included for comparison). Values for AT2018jbv were derived using the method described in Section 3.2, with the closest to peak modelled epoch ($\sim$ 7 d postpeak) epoch used an an initial value. The SLSNe-I events SN2018hti and SN2019neq from Z. H. Chen et al. (2023) are also displayed. SN2018hti's data has been smoothed for better visual clarity. One data point for AT2019cmw fit using LT *griz* and *Swift* UV data $\sim$ 14.5 d post-peak is significantly deviating from the general trend in both temperature and radius.

(2023) and A. Mummery et al. (2024), with our own arguments for this interpretation presented later in Section 4. We note that although we use these pre-peak data points for our models in Sections 5.3 and 6, if this assumption is not physically accurate for AT2019cmw it does not materially affect our overall conclusions.

Fig. 5 shows the evolution of AT2019cmw's temperature, radius and luminosity over time obtained using the above methods. As can be seen in Fig. 5, AT2019cmw has a temperature of $\sim 10^{4.45}$ K close to peak, and then steadily cools over the next $\sim$ 50 d. It then continues cooling at a slower rate to $\sim 10^{3.85}$ K at $\sim$ 300 d post-peak. Its radius appears to gradually increase/plateau post-peak, increasing from $\sim 10^{15.45}$ cm to $\sim 10^{15.65}$ cm. Its luminosity peaks at $\sim 10^{45.6}$ erg s^{-1}. The rate of luminosity decline

broadly follows its temperature evolution, steadily declining for the first $\sim$ 50 d before declining at a slower rate for the following $\sim$ 250 d to $\sim 10^{43.6}$ erg s^{-1}. By integrating our derived luminosities over time, we find that AT2019cmw emitted $\sim 1.7 \times 10^{52}$ erg between its first detection and our last modelled epoch at MJD 59041. This value was calculated assuming no host extinction and excludes emission outside of the period during which it was significantly detected, and so is a lower limit on the true total radiated energy. The derived temperatures, radii and luminosities for each fitted epoch of AT2019cmw's photometry are listed in Table A3.

In Fig. 5, we compare physical parameters derived from pseudo-blackbody SED fits for AT2019cmw to the blackbody evolution of 4 spectroscopically similar featureless TDEs, as well as the TDE-He event AT2020ddv, from the sample of E. Hammerstein et al. (2023). Temperatures, radii and luminosities for AT2020riz, AT2020qhs, AT2020ysg, and AT2020ddv were taken from E. Hammerstein et al. (2023). For AT2018jbv, we apply the same method, we used for AT2019cmw to its supplementary LT photometry detailed in Section 2.2, alongside ZTF, ATLAS, and *Swift* photometry from E. Hammerstein et al. (2023). We list AT2018jbv's blackbody parameters derived using this method in Table A4. We only consider these 4 featureless TDEs, as although other featureless TDEs have been catalogued by sample studies such as Y. Yao et al. (2023), they lack the comprehensive post-peak blackbody modelling needed to make the same comparison.

3.2.1 Possible deviation from blackbody

As can be seen in Fig. 5, we find a significantly lower blackbody temperature and higher blackbody radius for an epoch $\sim$ 14.5 d post-peak compared with optical-only fits at a similar time. In Fig. 6, we show blackbody SEDs fit to snapshots of interpolated photometry at the beginning, middle, and end of the period during which *Swift* UV data was gathered between 14.5 and 33.6 d post-peak in order to probe this further. We also show an SED-fit at 71.8 d post-peak to highlight the continuing evolution of AT2019cmw's SED. At 14.5 d post-peak luminosity in rest-frame, the *Swift* UV bands are underluminous compared with other bands at optical wavelengths assuming a blackbody SED. At 33.6 d post-peak, all bands appear consistent with a blackbody SED.

In case this behaviour was due to the presence of multiple emitting regions with differing temperatures and radii shortly post-peak, we attempted a multicomponent blackbody fit for the epochs detailed above. However, this did not improve the quality of our fits, suggesting that a single component is dominant in the optical/UV.

We discuss this potential UV underluminosity further in Section 7.4.

3.3 Post-peak colours

As seen in Fig. 7, AT2019cmw has a blue colour of < 0 mag close to peak across broadband filter pairs between *u* band and *z* band. It then begins to redden with time, with its *u-g* colour increasing significantly faster than colours between other observed optical bands in the first $\sim$ 50 d post-peak, before slowing to a rate more comparable with these other bands. As they appear spectroscopically similar and have comparable peak luminosities, we compare AT2019cmw's *g − r* colour with the 4 featureless TDEs from E.
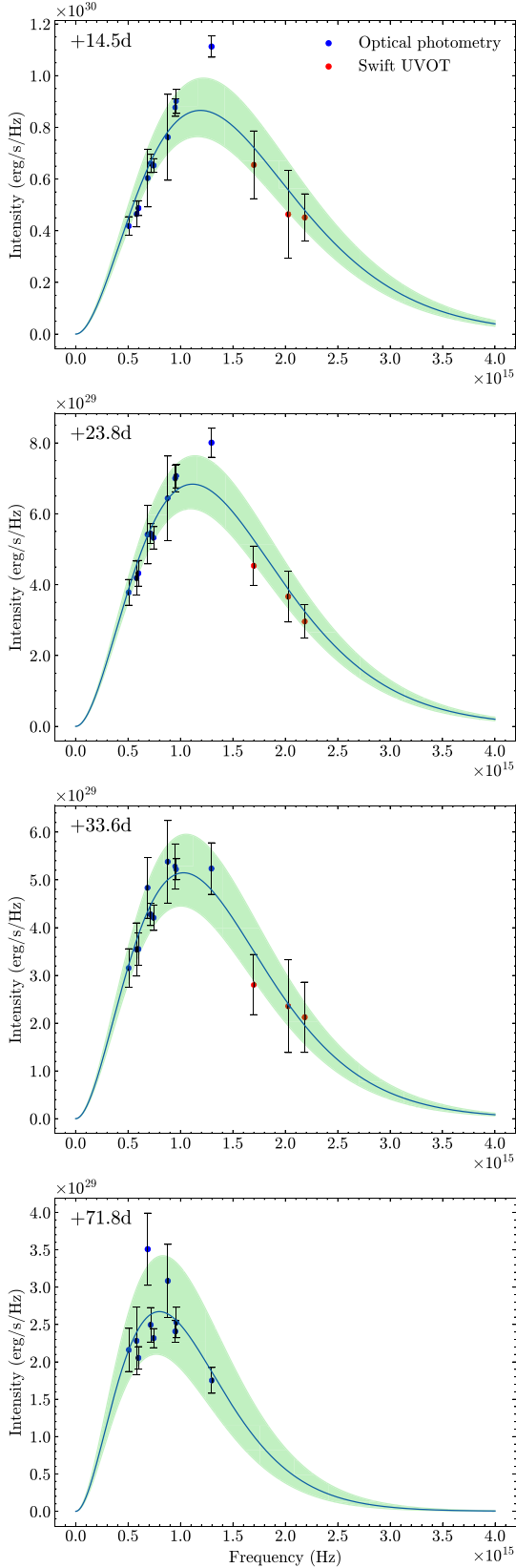
Figure 6. Blackbody SED fits to interpolated rest-frame multi-wavelength photometry for 14.5, 23.8, 33.6, and 71.8 d post-peak luminosity in rest frame. Fits are in chronological order from top to bottom. Optical and *Swift* UVOT photometry are indicated by blue and red points, respectively. The shaded region above and below the curve represents the 1σ confidence interval of our fit.
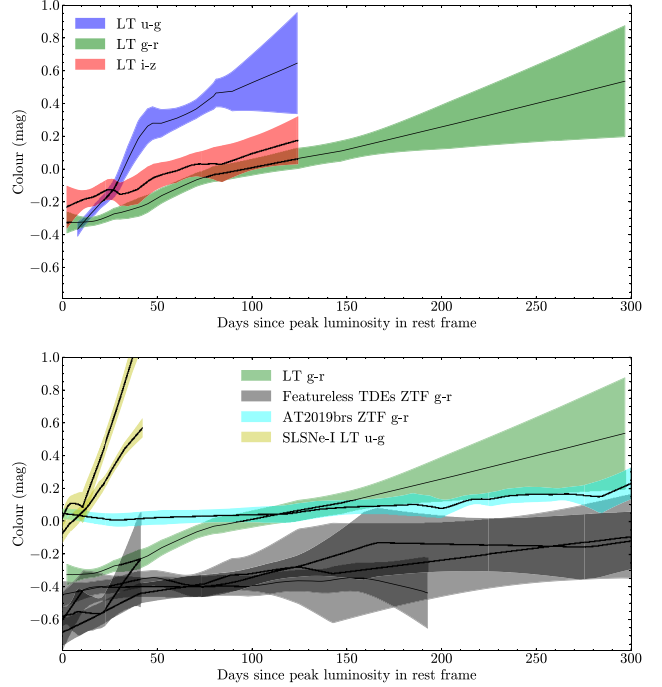
Figure 7. Top: Observed LT $u-g$, LT $g-r$, and LT $i-z$ colours for AT2019cmw in the first 300 d since peak luminosity in its rest-frame. **Bottom:** LT $g-r$ colour of AT2019cmw plotted against ZTF $g-r$ colours of the 4 featureless TDEs presented by E. Hammerstein et al. (2023) and the luminous ANT AT2019brs from P. Wiseman et al. (2025) since peak luminosity in each transient's respective rest-frame. For comparison, we also show LT $u-g$ colours of the SLSNe-I events SN 2018hti and SN 2019neq from Z. H. Chen et al. (2023). As these events were at redshifts of $z = 0.063$ and $z = 0.1075$ respectively, their $u-g$ colours provide a more accurate rest-frame comparison than their $g-r$ colours to the plotted higher redshift TDEs and ANTs at $z \sim 0.3$-0.5. Shaded regions show errors propagated from Lowess interpolated photometry.

Hammerstein et al. (2023) in the first 300 d post-peak in each transient's respective rest frame. Whilst they arguably show some colour evolution, none of these other events show the same significant change that AT2019cmw does, and maintain a colour of ≤ 0 throughout their evolution. AT2019cmw by comparison reddens in its LT photometry from a $g-r$ colour of ~ -0.35 mag near-peak to ~ 0.50 mag at late times. Compared with the luminous ANT AT2019brs (P. Wiseman et al. 2025) AT2019cmw appears ~ 0.3 mag bluer at peak, whereas at late times it is comparable in colour. AT2019cmw is also ~ 0.3 mag bluer than the SLSNe-I SN 2018hti and SN 2019neq (Z. H. Chen et al. 2023) at peak, and reddens significantly slower than both post-peak. See Section 7.3 for a more detailed comparison of the evolution of inferred black-body parameters between AT2019cmw and the featureless TDEs from E. Hammerstein et al. (2023).

3.4 Host Galaxy

rizy PS1 photometry of AT2019cmw's host is listed in Y. Yao et al. (2023). The host galaxy is only marginally detected in the Pan-STARRS1 *g*-band image. To recover the magnitude in this band, forced aperture photometry at the host location was performed using a 2 arcmin radius, with a small aperture correction (measured using the *r*-band image) applied. From this, we find a *g*-band magnitude of $g = 22.57 \pm 0.29$ for AT2019cmw's host.

Combined with the photometry from Y. Yao et al. (2023), this shows it to be a red galaxy. We show a PS1 *gri* composite image of AT2019cmw's host in Fig. 1.

AT2019cmw's host SED was fit in the sample study from Y. Yao et al. (2023), in which they find it to be consistent with being a normal non-active galaxy.

The lack of any detected variability in NEOWISE photometry at the source location from 1081.5 d prior to and 829.5 d post peak luminosity in rest-frame means that any IR-reflecting material that may exist out to 2×10^{18} cm from the event, such as a dusty AGN torus, was not significantly detected (using $d = ct$). AT2019cmw may begin to display rising IR emission in the future, as radiation from the event reaches more distant IR-reflecting material. This is not particularly constraining. N. Jiang et al. (2021), for example, detected IR variability in 23 optically selected TDEs; however, they were all at significantly lower redshift than AT2019cmw.

We fit a gaussian line profile to the host spectrum at the location of Hα in order to attempt to measure the galaxy's star formation rate (SFR). The FWHM of this gaussian, 6.9 Å, corresponds to the FWHM resolution for the LRIS 400/8500 grating using a 1 arcmin slit[3]. This yielded a 3σ flux upper limit of $\lesssim 3.5 \times 10^{33}$ erg s^{-1}. This corresponds to an approximate 3σ upper limit on the star formation rate of $\lesssim 0.3\,\mathrm{M_\odot yr^{-1}}$ using the relation from R. C. Jr Kennicutt, P. Tamblyn & C. E. Congdon (1994), and a specific star formation rate of $\lesssim 3.7 \times 10^{-12}\,\mathrm{yr^{-1}}$ for a stellar mass of $10^{10.88}\,\mathrm{M_\odot}$ (Y. Yao et al. 2023).

3.4.1 Host-transient offset

In order to quantify the offset between the transient and its host galaxy, we compare the measured position of the transient in a host-subtracted LT image with the position of the host in PS1 reference imaging. To do this, we chose a high quality LT *i*-band image with good seeing and low moon contamination from 2019-06-08, and a stacked *i*-band PS1 cutout of the host galaxy. *i*-band images were chosen as the host galaxy has the highest S/N in this band.

To perform the subtraction, the LT image was first aligned with the PS1 reference image using SWARP. PSFs for both images were measured using PSFEx (E. Bertin 2013), and each image was convolved with the PSF of the other using SOURCE EXTRACTOR. The alignment of the convolved images is refined using SCIPY's NDIMAGE.SHIFT function. We then normalise the images for subtraction, using a chosen subset of foreground reference stars that pass a number of quality cuts.

After subtraction, we measure the difference in the position of the transient and the host in subtracted and reference images using SOURCE EXTRACTOR. A final correction to this difference was then applied using the mean of the offset of the foreground reference stars between both images. The error of the position of both the transient in host-subtracted LT images and the host in PS1 was found using the scatter in the position offset of foreground reference stars between both images.

Using this method, an offset of 0.195 PS1 pixels was found between AT2019cmw and its host, and a scatter of 0.449 pixels using foreground stars. This corresponds to an offset of 0.049 arcmin and a scatter of 0.112 arcsec, and thus 0.57 kpc with a scatter of
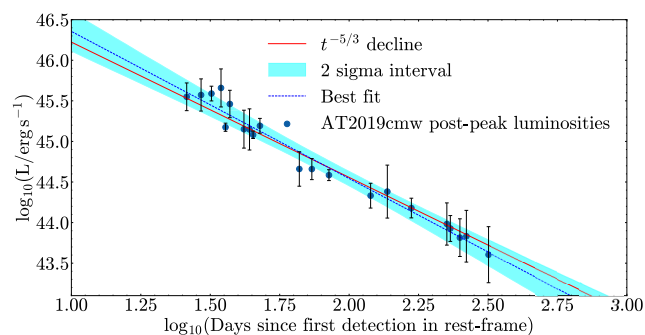
[3] https://www2.keck.hawaii.edu/inst/lris/dispersive_elements.html

Figure 8. Log-space plot of AT2019cmw's inferred post-peak luminosities from Fig. 5 (points) fit to a power-law decline (dashed line) with the 2σ confidence interval on the fit overlaid (shaded region). A $t^{-5/3}$ power-law decline has also been plotted for comparison (solid line).

1.31 kpc at a redshift of $z = 0.519$. We do not see any significant offset between the transient and its host-galaxy, and thus consider the transient as nuclear.

3.5 X-ray and radio non-detections

Our X-ray flux upper limit, as detailed in Section 2.3, translates to an X-ray luminosity upper limit of $L_X \lesssim 2 \times 10^{43}$ erg s^{-1} between 0.3 and 15.2 keV, between ~ 12 and ~ 54 d post-peak, in AT2019cmw's rest-frame. This is not particularly constraining on the presence of X-ray emission. For example, in the study by E. Hammerstein et al. (2023) for TDEs with a redshift of $z \leq 0.075$ they find six TDEs with $L_X \leq 10^{42}$ erg s^{-1} and 7 TDEs with $L_X \geq 10^{42}$ erg s^{-1}. However, some of the TDEs in their sample considered 'X-ray bright' would be detected at AT2019cmw's redshift at the depth of our observations. AT2020ddv, for instance, has a *Swift* XRT X-ray luminosity of $\gtrsim 3 \times 10^{43}$ erg s^{-1} at a similar time to AT2019cmw post-peak. In addition to this, AT2020ddv is almost an order of magnitude less luminous at optical/UV wavelengths than AT2019cmw. At the time of our observations, the ratio between AT2019cmw's derived blackbody luminosity and its X-ray luminosity upper limit was $\sim 50 - 100$. As can be seen in Fig. 8 from E. Hammerstein et al. (2023), this would place it near the upper end of their L_{BB}/L_X distribution for X-ray detected TDEs. In their sample, at a similar time post-peak to our *Swift* XRT observations 6 TDEs had L_{BB}/L_X between ~ 1 and ~ 50, and 2 showing L_{BB}/L_X between ~ 100 and ~ 300. This suggests that AT2019cmw was not particularly X-ray luminous at the time of our observations.

Assuming a spectral shape of $F_\nu \sim \nu^{-1}$ for our *K*-correction, our VLA *C*-band flux upper-limit of $< 4.5\,\mu$Jy corresponds to a luminosity upper limit of $\nu L_\nu < 2.8 \times 10^{38}$ erg s^{-1} between 4–8 GHz 1474.86 d after first detection (970.94 d in rest frame). As seen in the sample paper from Y. Cendes et al. (2024), the majority of optically selected TDEs are not particularly radio-loud, with many events being detected at luminosities below our detection limit at a similar time post first-detection. However, they show that a subset of TDEs are extremely radio-luminous due to on-axis relativistic jetted emission. Swift J164449.3 + 573451 (Y. Cendes et al. 2021) for instance was detected at a luminosity over two orders of magnitude above our detection limit for AT2019cmw's redshift. This places tight constraints on the presence of any on-axis relativistic jetted emission in AT2019cmw. We discuss this further in Section 7.5.

4 PHYSICAL ORIGIN SCENARIOS FOR AT2019CMW

In this section, we consider several different physical interpretations in order to explain AT2019cmw's observed characteristics.

AT2019cmw has been previously classified and analysed as a featureless TDE in the sample studies from A. Mummery et al. (2024) and Y. Yao et al. (2023), and appears spectrally similar to the featureless TDEs from E. Hammerstein et al. (2023), as we show in Fig. 4 where AT2018jbv is plotted for comparison. However, it lacks a concrete 'smoking gun' that definitively pins down its physical origin, such as detected X-ray or radio emission. As a result, we briefly consider here some potential alternative physical interpretations for AT2019cmw's observed characteristics.

4.1 Extreme supernova

Despite its host's low rate of star formation, as detailed in Section 3.4, its significant temperature evolution post-peak motivates us to consider an extreme SLSN scenario for AT2019cmw.

The most extreme magnetar spin-down powered models of SLSN-I from T. Sukhbold & S. E. Woosley (2016) generate a peak luminosity of $L = 2 \times 10^{46} \mathrm{erg\,s^{-1}}$, which could possibly explain our observations. However, as seen in Fig. 5, at peak AT2019cmw is significantly hotter than typical SLSNe. Additionally, SN2020hti was highlighted by Z. H. Chen et al. (2023) to be a high-temperature outlier in their sample of SLSN-I events, AT2019cmw displays significantly higher temperatures at all comparative epochs. Although its radius evolves slower than the SLSN-I events seen in Fig. 5, AT2019cmw also displays a plateau in its blackbody radius for at least 300 d in rest frame, which could be explained by the photosphere receding into the expanding ejecta of a supernova as it becomes optically thin.

However, the strongest line of evidence against an SN interpretation is the persistently featureless nature of AT2019cmw's spectra, even out to late times. In the case of a supernova, as the photosphere recedes, the radiation would begin to pass through optically thin ejecta and a nebular spectrum would start to be produced. This can be seen in Fig. 4, with SN 2010gx (A. Pastorello et al. 2010) showing more prominent spectral features as it evolves, whereas AT2019cmw stays featureless. Therefore, it is unlikely that AT2019cmw's properties can be explained using a peculiar SLSN scenario.

4.2 Peculiar AGN flare

As we state in Sections 3, 3.3, and 3.4, AT2019cmw's blue UV colour at peak, featureless spectra, as well as the source location's NEOWISE nonvariability and host SED consistent with a normal non-active galaxy (Y. Yao et al. 2023) are evidence against it being the result of an AGN flare. However, due to its nuclear location and high luminosity compared with the majority of previously discovered TDEs and SNe to date, we consider this possibility.

Quasars, for example, have been observed at luminosities significantly higher than AT2019cmw at peak from low to high redshifts (X. Shen et al. 2020). However, as can be seen in the composite spectrum from D. E. Vanden Berk et al. (2001) shown in Fig. 4, quasars show a combination of broad and narrow emission lines in their spectra. This is unlike our spectral sequence seen in Fig. 4, which remains a featureless continuum for its entire evolution. Our spectra are also unlike those of previously observed Seyfert

galaxy nuclei, which also show characteristic emission features (J. R. Mullaney & M. J. Ward 2008).

Blazars however have been seen to display predominantly featureless continua in the optical (D. DuPuy et al. 1969; M. Stickel et al. 1991; P. Goldoni et al. 2021), and are also preferentially seen in massive early type host galaxies (C. M. Urry et al. 2000). However, in the optical their SEDs are dominated by synchrotron emission and appear as a power-law continuum (M. Fiorucci, S. Ciprini & G. Tosti 2004; G. Ghisellini et al. 2011), rather than the blackbody SEDs which we observe for AT2019cmw as highlighted in Fig. 6.

It is possible that AT2019cmw is a peculiar AGN 'turn-on' event in a previously quiescent galaxy. L. Yan et al. (2019), for example, observed a prompt AGN turn-on event in the previously quiescent galaxy SDSS1115+0544. However, there are significant observational differences between AT2019cmw and this event. They note the AGN turn-on event in SDSS1115+0544 is unlike previously observed SNe and TDEs due to its strong, persistent UV emission years after the initial 'turn-on', indicative of a newly formed accretion disk. This presents as a steep slope into the UV in their photometry and spectroscopy blueward of ~ 4000 Å. As seen in Fig. 4, we instead observe strong UV flux at early times that fades to show a quiescent galaxy spectrum at late times. Additionally, they observe the formation of prominent hydrogen, oxygen and iron emission lines during the flare, in contrast to AT2019cmw's persistent featureless spectra.

Another notable class of events as a comparison are ANTs, which appear to display smooth light-curve evolution post-peak (P. Wiseman et al. 2025), somewhat similar to AT2019cmw. Although P. Wiseman et al. (2025) hypothesize that ANTs are potentially the result of TDEs of intermediate to high mass stars, they appear spectroscopically similar to AGN. P. Wiseman et al. (2025) note that the events in their sample ubiquitously show broad AGN-like Balmer emission features. The related subclass of 'Extreme Nuclear Transients' (ENTs) presented by J. T. Hinkle et al. (2025), which they also hypothesize resulted from TDEs of intermediate to high mass stars, also appear to display broad Mg II emission. J. T. Hinkle et al. (2025) state that as this feature is commonplace in AGN spectra, this could be the result of a pre-existing reservoir of gas around the SMBH. These events appear distinct from AT2019cmw, which displays featureless spectra throughout its entire observed evolution.

Due to AT2019cmw's observable characteristics being inconsistent with being the result of an AGN-related phenomenon, we consider it inconsistent with being the result of an AGN flare.

4.3 Tidal disruption event

AT2019cmw appears nuclear in its host. Our measured offset of 0.049 arcmin and a scatter of 0.112 arcsec, as detailed in Section 3.4.1, is consistent with the offset of ≤4 arcmin for TDEs selected by the ZTF sample studies from S. Velzen et al. (2021) and E. Hammerstein et al. (2023). As AT2019cmw's host also displays a lack of detected AGN activity, and AT2019cmw itself does not show any AGN-like or SN-like spectral features, we return to the scenario of a TDE to explain its observed properties.

As can be seen in Figs 5 and 7, AT2019cmw cools significantly post-peak compared to the featureless TDEs from E. Hammerstein et al. (2023) that display similar featureless spectra. However, as peculiar TDEs and candidate-TDEs have also displayed similar post-peak temperature evolution, we do not consider this to be evidence against a TDE interpretation for AT2019cmw. For

example, the candidate featureless TDE Dougie (J. Vinkó et al. 2014) as well as the fast evolving TDE AT2020neh (C. R. Angus et al. 2022), both discussed further in Section 7.3, appear to cool significantly post-peak.

S. Gezari (2021) make the argument that the *NUV-r* colour of a TDE at peak is a potentially robust method of photometrically differentiating TDEs from other transients such as AGN and SNe. AT2019cmw displays significant reddening of its *uvw2 − r* colour post-peak. When measuring colours from interpolated light-curves of significant detections, from 14.1 and 33.8 d post-peak in its rest-frame the *UVW2 − r* colour reddens from 0.37 mag to 0.73 mag with a consistent absolute magnitude in *UVW2* of $M < -22$. This would put it in-between the regime of TDEs and AGN. Fig. 10 from S. Gezari (2021) for instance shows that TDEs appear to have a peak $NUV - r$ colour $\lesssim 0$ mag, whereas AGN have a colour of $\gtrsim 1$ mag, and SNe a colour of $\gtrsim 0.5$ mag. However, as it was rapidly reddening in $u - g$ from at least ~ 6 d before our first *UVW2* detection, it is likely that at peak its colour is close to $UVW2 - r = 0$ mag.

In Fig. 8, we fit a power-law decline to our derived post-peak bolometric luminosities of AT2019cmw from Section 3.2 to determine the slope index of the decline α, with the time of disruption (t_0) set at the time of the first ZTF *g*-band forced photometry detection. At the 1σ level, we find a value of $\alpha = 1.81^{+0.07}_{-0.07}$. Within 2σ, we find AT2019cmw's rate of decline to be consistent with the $t^{-5/3}$ decline for TDEs predicted using theoretical fallback accretion rates from M. J. Rees (1988) and E. S. Phinney (1989). It should be noted that AT2019cmw's first photometric detection is almost certainly after the true t_0. Varying t_0, we find that AT2019cmw's rate of decline is still consistent with a $t^{-5/3}$ decline within 2σ if t_0 is set to 4 days pre-first detection.

AT2019cmw displays a blue colour and high temperature at peak, and its post-peak luminosity decline rate is consistent with a $t^{-5/3}$ power law. Combined with its featureless spectra and nuclear location in its host with a lack of any detected AGN activity, this motivates us to interpret AT2019cmw as a peculiar featureless TDE of the class defined by E. Hammerstein et al. (2023).

5 REDBACK 'COOLING ENVELOPE' MODEL

In order to derive parameters such as the mass of the disrupted star and disrupting black hole, we fit our photometry of AT2019cmw using the open-source software package REDBACK (N. Sarin et al. 2024). We use the TDE cooling envelope model (B. D. Metzger 2022b) using the DYNESTY sampler (J. S. Speagle 2020) wrapped with BILBY (G. Ashton et al. 2019). One advantage of this model compared with other widely used TDE models such as from B. Mockler et al. (2019), is it is not agnostic to the mechanism of energy production from the fallback of stellar material. As described in N. Sarin & B. D. Metzger (2024), it is based on the assumption that the super-Eddington fallback of stellar material onto a black hole during a TDE forms a pressure-supported envelope after the first fallback time, which then cools and undergoes Kelvin–Helmholtz contraction before forming a disk at later times. As such, this model is potentially able to explain how some TDE systems do not brighten in X-rays (Y. Yao et al. 2022) and radio (Y. Cendes et al. 2024) until long after the optical/UV peak, which may apply in the case of AT2019cmw with its X-ray non-detection close to peak and relatively non-constraining radio upper limit at late times.
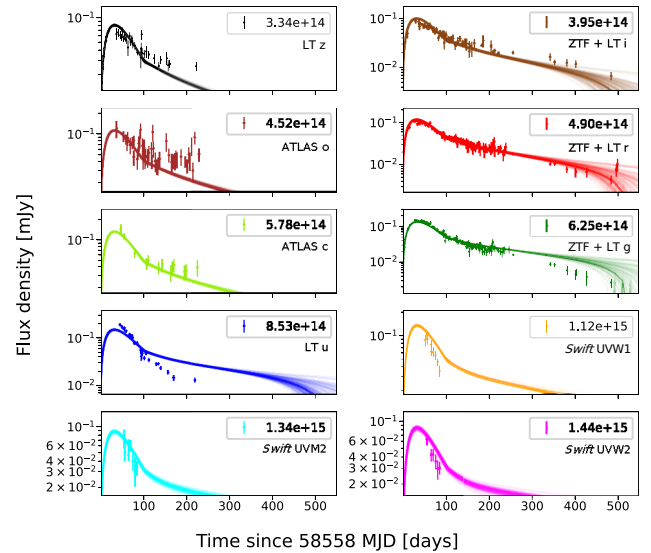

Figure 9. ATLAS, ZTF, LT, and *Swift* photometry detailed in Section 2 in ascending order of frequency, overlaid with light-curves generated from 100 random draws from the posterior. ZTF and LT light-curves in the same respective bands have been merged. The rest-frame frequency in Hz, as well as the observed photometric filters, for each wavelength bin fit in our model are displayed in the upper-right of each box.

We adopt the method used by N. Sarin & B. D. Metzger (2024) to model their sample of TDEs. The predicted fallback timescale of the system is defined by equation (3) from N. Sarin & B. D. Metzger (2024), which they adapt from equation (51) from N. Stone, R. Sari & A. Loeb (2013):

$$t_{fb} \approx 58\mathrm{d}\left(\frac{\kappa}{0.8}\right)^{-3/2} m_*^{1/5} M_{\mathrm{bh},6}^{1/2}, \tag{1}$$

in which m_* is the mass of the disrupted star in $M_\odot$ and $M_{\mathrm{bh},6}$ is the mass of the disrupting black hole in $10^6 M_\odot$. κ is a constant related to the stellar binding energy, which N. Sarin & B. D. Metzger (2024) set to 0.8.

Before the envelope formation time in the model as defined by χt_{fb}, with χ accommodating for model uncertainties in the envelope formation time, we use a phenomenological broken power law to fit the transient's photometry prior to and shortly after peak. The light-curve evolution during this time is defined by the Equation 5 from N. Sarin & B. D. Metzger (2024):

$$F(\nu, t) = A_\nu \left(1 - e^{t/t_{peak}}\right)^{\alpha_1} \left(\frac{t}{t_{peak}}\right)^{-\alpha_2}. \tag{2}$$

A_ν represents a normalisation for each specific frequency in the model, α_1 and α_2 represent the rise and decline indices prior to and post-peak respectively. After $t = \chi t_{fb}$, the phenomenological model is smoothly connected to the cooling envelope model.

The uncertainties quoted for our model posterior distributions in this section are 95 per cent credible intervals.

5.1 Multiband photometry fit

We use a broad set of priors for all parameters and run until convergence. Fig. 9 shows light-curves from our model fits plotted against AT2019cmw's photometry. Around peak, the power-law fit is a good match to our data. Although as the model progresses to late times the *g* band is somewhat overestimated, and *i* band
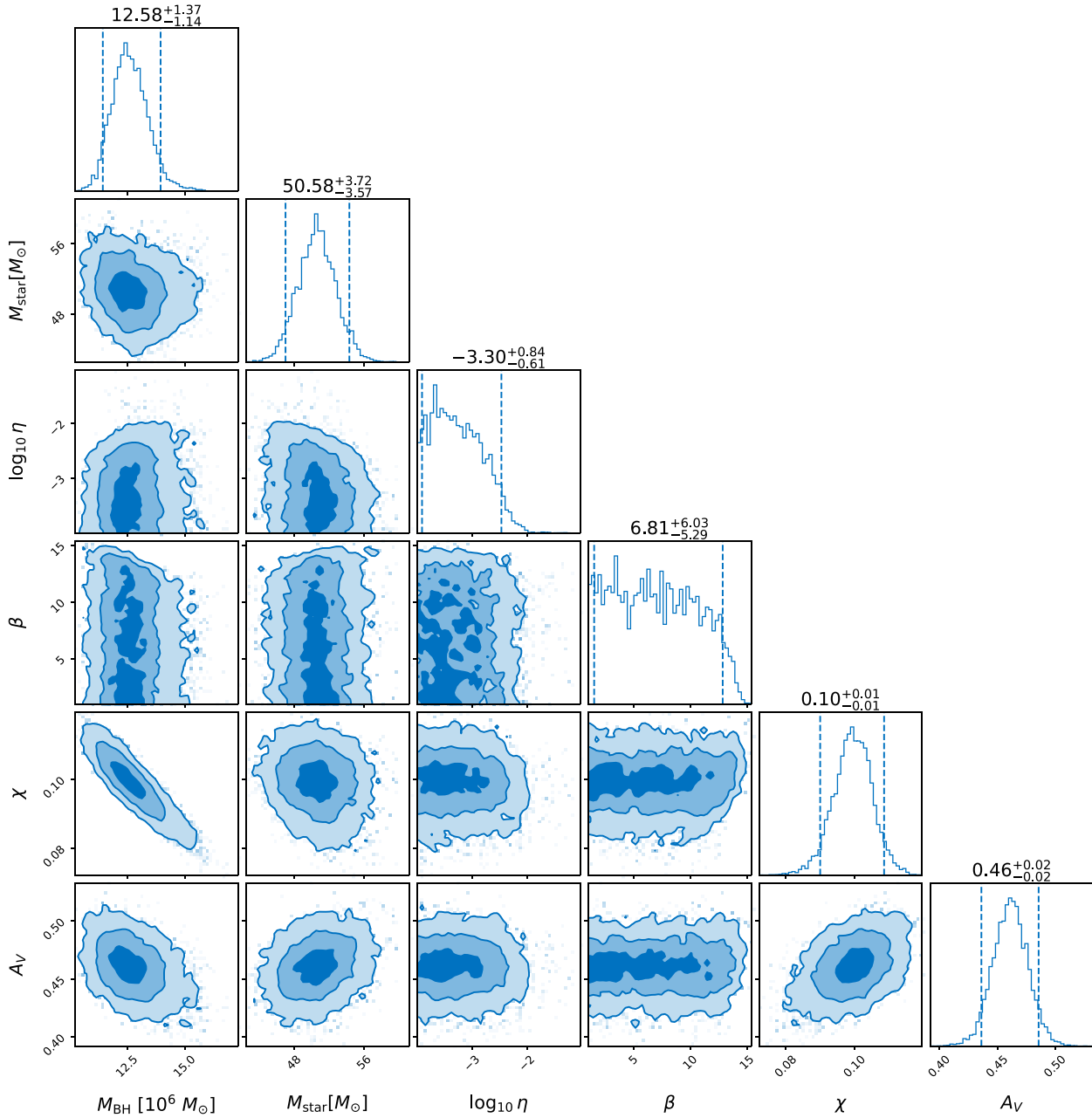
Figure 10. Inferred parameters from our 'cooling envelope' model fit to the multiband photometry shown in Fig. 9. Plot made using CORNER (D. Foreman-Mackey 2016).

and z band are underestimated, likely due to the fact that the photospheric cooling seen in AT2019cmw is not predicted to this extent by the model from B. D. Metzger (2022b). The u-band and *Swift* UV bands are moderately well fit close to peak, but are significantly overestimated as the model progresses to later times. This is discussed further in Section 5.2.

Parameters extracted from this model are displayed in Fig. 10 and Table 2. Our model fits output a disrupted star mass of $M_* = 50.58^{+3.72}_{-3.57}\,M_\odot$, a disrupting black hole mass of $M_{bh} = 1.258^{+0.137}_{-0.114} \times 10^7 M_\odot$ and a penetration factor of $\beta = 6.81^{+6.03}_{-5.29}$, with $\beta = r_t/r_p$, the ratio between the radius of the tidal disruption and the periapsis of the in-falling debris respectively. We

also find an SMBH feedback efficiency of $\eta = 5^{+30}_{-4} \times 10^{-4}$ and an internal extinction of $A_V = 0.46^{+0.02}_{-0.02}$ mag. We note that these uncertainties are underestimations of their true values, as they do not take into account systematic errors or model misspecification. The complete posterior distribution extracted from this model is presented in Fig. B1.

Although our estimate of M_{bh} is of the same order of magnitude, it is significantly different from the mass of $M_{bh} = 6.31^{+7.82}_{-3.50} \times 10^7 M_\odot$ found by A. Mummery et al. (2024) using a late-time thin-disc emission model, and the mass of $M_{bh} = 8.71^{+14.10}_{-5.40} \times 10^7 M_\odot$ found by Y. Yao et al. (2023) using host galaxy scaling relations, with M_{gal} derived from SED fitting of host pho-

Table 2. Summary of relevant parameters output by our model fits from Sections 5.1, 5.3, and 6. Uncertainties for parameters from the cooling envelope model are 95 per cent credible intervals, whereas for the reprocessing outflow model we show 1σ errors. A full list of output parameters from our cooling envelope model fits can be seen in Figs B1 and B2.

Cooling envelope model (multiband fit)	
M_{BH} ($10^6 M_\odot$)	$12.58^{+1.37}_{-1.14}$
M_* ($M_\odot$)	$50.58^{+3.72}_{-3.57}$
$\log_{10}\eta$	$-3.30^{+0.84}_{-0.61}$
β	$6.81^{+6.03}_{-5.29}$
χ	$0.10^{+0.01}_{-0.01}$
t_0 (MJD)	$58555.63^{+1.38}_{-1.92}$
A_V (mag)	$0.46^{+0.02}_{-0.02}$
Cooling envelope model (bolometric fit)	
M_{BH} ($10^6 M_\odot$)	$0.24^{+0.20}_{-0.14}$
M_* ($M_\odot$)	$75.30^{+21.36}_{-36.84}$
$\log_{10}\eta$	$-2.02^{+1.73}_{-1.73}$
β	$51.68^{+42.51}_{-42.91}$
χ	$0.53^{+0.35}_{-0.18}$
t_0 (MJD)	$58533.68^{+13.22}_{-13.24}$
Reprocessing-outflow model ($10\,000\,\mathrm{km\,s^{-1}}$)	
M_{ej} ()	142 ± 10

tometry. However, we note that for both of these values of M_{bh} the uncertainties quoted are at the 1σ level.

By generating a predictive posterior distribution from 1000 samples of our results, we also derive proxy X-ray luminosities predicted by the model for AT2019cmw. The X-ray luminosities predicted by our model remain on a plateau at $\sim 5 \times 10^{43}$ erg s^{-1} until ~ 100 d post-envelope formation. They are then predicted to rise and approach the Eddington luminosity of the system as the envelope terminates and the SMBH accretion rate increases (B. D. Metzger 2022b), reaching $\sim 2 \times 10^{46}$ erg s^{-1} in our model ~ 1100 d post-first fallback. These proxy X-ray luminosities are presented in Fig. C3.

Our *Swift* XRT observations, detailed in Section 2.3, were taken between ~ 2 d prior to and ~ 24 d after χt_{fb} in the source frame. When comparing the predicted plateau at this phase of evolution, our observed *Swift* X-ray luminosity upper-limit of $\lessapprox 2 \times 10^{43}$ erg s^{-1} is significantly lower than that predicted by our model. However, as this occurs during the 'cooling envelope' phase in our model, the predicted X-ray emission would only be detectable from select viewing angles roughly aligned with the black hole's axis of rotation (N. Sarin & B. D. Metzger 2024) and thus may not have been visible along our line of sight.

5.2 Multiband fit caveats

As seen in Fig. 9, a phenomenological power-law fit before and shortly after peak followed by a fit using the cooling envelope model describes the behaviour of our optical and UV light-curves reasonably well. However, at later times, the model underestimates the rate of reddening that we observe, leading us to underestimate the observed rate of cooling from Section 3.2 in our fit. One possible explanation for this is that, as can be seen in Fig. 9, slower fading redder bands have better coverage and S/N at late times. As a result, redder bands could have been more

significantly weighted in the fit compared to bluer bands, causing the latter's luminosity to be overestimated at late times. Although the model generally does well at predicting AT2019cmw's photometric evolution, the discrepancy between the colour of our observations and the model fit at later times, as well as the fact that we observe an increase in photometric radius in Section 3.2, suggest that our value of η (the SMBH feedback efficiency) in this fit may be an underestimate.

A significant caveat also applies to our derived value of M_{bh} from Section 5.1. As stated in section 3.1.1 of B. D. Metzger (2022b), close to peak the bolometric luminosity in the cooling envelope can be considered as $L = L_{edd} + L_{fb}$, where L_{edd} is the Eddington luminosity of the envelope and L_{fb} is an additional luminosity contribution from the fallback of stellar material. At later times, the bolometric luminosity in the model approaches $L \approx L_{edd}$, which can be used to constrain the SMBH mass. Randomly sampling the posterior distribution from our fit, we find that the model predicts $L_{edd} \approx 10^{45.3}$ erg s^{-1} at ~ 300 d post-envelope formation. In reality, our blackbody fits from Section 3.2 show that the bolometric luminosity decreases to $\sim 10^{43.6}$ erg s^{-1} ~ 300 d post-peak. This implies that in our fits from Section 5.1 our value of M_{bh} may be significantly overestimated, as these fits significantly overestimate the bolometric luminosity (and thus L_{edd}) at later times. The predicted blackbody characteristics of our model fit from Section 5.1 are presented in Fig. C1.

As stated in Section 5.1, our best fitting model converges to a penetration factor of $\beta = 6.81^{+4.34}_{-4.01}$. Although there is a large uncertainty on this value, it suggests that this event may be a 'high-penetration' TDE. Using the following equation for the radius of tidal disruption from J. G. Hills (1975), $r_t = \left(\frac{M_{bh}}{M_*}\right)^{1/3} R_*$, the Schwarzschild radius as defined by $R_s = \frac{2GM}{c^2}$ and the approximate mass-radius relation for main sequence stars as defined by $R_* \approx \left(\frac{M_*}{M_\odot}\right)^{4/5} R_\odot$, we find a periapsis, r_p, of the stellar material of $r_p = 3.99^{+5.72}_{-1.55} R_s$. Within this range, general relativistic precession could be significant enough to cause infalling debris stream to intersect itself when it completes an orbit (Z. L. Andalman et al. 2022). The resulting stream–stream collisions would add an additional source of radiation that is not currently taken into account in the cooling envelope model.

In the same vein, as stated by B. D. Metzger (2022b), κ weakly depends on β (J. Guillochon & E. Ramirez-Ruiz 2013; N. Stone et al. 2013). In the cooling envelope model, however, N. Sarin & B. D. Metzger (2024) and B. D. Metzger (2022b) fix the value of κ to 0.8 as an approximation, which corresponds to $\beta = 1$ for a polytropic star with $\lambda = 5/3$, even though β is allowed to vary in the model. Considering equation (1), this implies that the fallback time may be inaccurate. This is supported by our estimated value of $\chi \sim 0.1$, which implies that the fallback time found using equation (1) may be a significant overestimate. As is discussed in Appendix C of N. Sarin & B. D. Metzger (2024), varying κ can also significantly affect estimates of the mass of the star and disrupting black hole. If the true physical value of κ is higher, then this could mean that our models estimates of M_* and M_{bh} are underestimated and overestimated respectively. Our results highlight a degeneracy between κ and the inferred masses. However, properly accounting for this degeneracy requires modelling how κ depends on the star mass and β, which is not properly included in the REDBACK implementation of the cooling envelope model. Leaving κ as a free parameter will artificially broaden the posterior, but not correctly capture the physics,
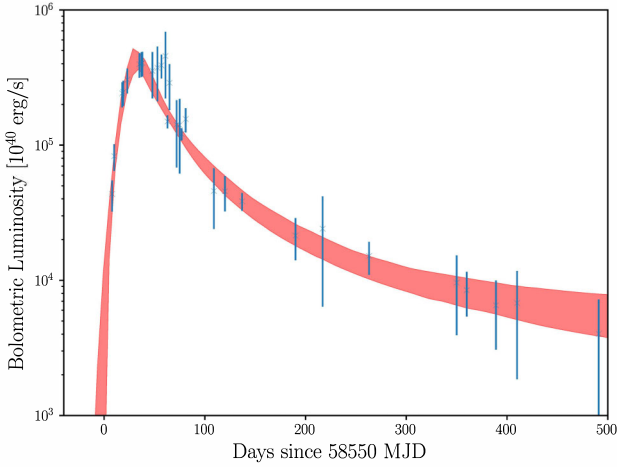
Figure 11. 1σ confidence interval of the cooling envelope model, shown as a shaded error region, fit to AT2019cmw's derived blackbody luminosities from Section 3.2, shown as vertical error bars.

muddying the physical meaning of some of the implicitly derived quantities in the model. As such, we chose to keep κ fixed in our modelling. With a different value of κ, such as 0.4 as chosen by N. Sarin & B. D. Metzger (2024), we would expect a similar scaling for our derived values of M_* and M_{bh} of ~ 2 times larger and ~ 4 times smaller respectively. This would not qualitatively affect our findings from Section 5.1.

As seen in Fig. 10, our model fits estimate an internal extinction of $A_V = 0.51^{+0.02}_{-0.02}$ mag. In Section 3.2.1 we describe our observations of a u-band excess and a potential UV underluminosity at early times, which we go on to discuss in Section 7.4, as being potentially due to unseen absorption features in the UV. As a result, our estimate of host extinction, and thus the luminosity of the transient in the model, may be an overestimate. Combined with the assumption of $\kappa = 0.8$, it is likely that the disrupted star mass in the model is somewhat overestimated.

5.3 Bolometric fit

In order to further probe AT2019cmw with the cooling envelope model, we again use the method used in Section 5.1 to fit our multiband photometry. However, we instead fit AT2019cmw's derived blackbody luminosities from Section 3.2. As our input data for this model is achromatic, we cannot constrain the internal extinction as was done in Section 5.1, and so assume $A_V = 0$ mag. As a result, estimates of other parameters from this model are unaffected by any possible overestimation of this value. The model fit to our derived blackbody luminosities is shown in Fig. 11, and key extracted parameters are presented in Table 2. The complete list of parameters extracted from this model is presented in Fig. B2.

Using this fit, we estimate a disrupted star mass of $M_* = 75.30^{+21.36}_{-36.84} M_\odot$. Although our uncertainties are larger here, likely due to us only using epochs with >3 photometric data points as input rather than all of our photometry, this is consistent with the disrupted star mass found by our multiband fits in Section 5.1. As such, this shows that a disrupted star mass in the tens of solar masses is favoured to explain AT2019cmw's characteristics in the context of the cooling envelope model. This would be the case even if the masses of the disrupted star found by our Redback

model fits are overestimated by several times compared to the true value (such as if the true value of κ is significantly different from 0.8). This is an unprecedentedly high mass for a tidally disrupted star and, if accurate, could have far-reaching implications for our understanding of the environments surrounding SMBHs. This will be discussed further in Section 7.1.1.

For the disrupting black hole in this model we find a mass of $M_{bh} = 2.4^{+2.0}_{-1.4} \times 10^5 M_\odot$. This is almost 2 orders of magnitude smaller than the estimate made by our model from Section 5.1. As stated in Section 5.2, this may be due to the assumption in the cooling envelope model that at later times $L \approx L_{edd}$. One possible implication in the context of the cooling envelope model is that at later times, if such an envelope is in fact present, it may be radiating at a rate significantly below L_{edd}. This would have the effect of skewing our model's value of M_{bh} to a lower value. A similar discrepancy was also noted by A. Hajela et al. (2025) when discussing their cooling envelope fit of ASASSN-15oi, which displayed a thermal bolometric luminosity of $L \sim (0.1\text{-}0.3)L_{edd}$ at a time when the cooling envelope model predicts $L = L_{edd}$.

Also, curiously, our bolometric luminosity fit is broadly better at predicting the atypical blackbody behaviour that we observe in Section 3.2 than our fits detailed in Section 5.1. Despite the lack of colour information in the input data, our model fit generally predicts a photospheric temperature decrease and radius increase/plateau in the first ~ 300 d post-first fallback. These predicted blackbody characteristics are presented in Fig. C1.

The discrepancy between our cooling envelope model fits will be discussed further in Section 7.2.

6 REPROCESSING-OUTFLOW MODEL

We also consider an alternate reprocessing-outflow model, using the method outlined in T. Matsumoto & T. Piran (2021). In contrast to the cooling envelope model discussed in Section 5.1, this model operates under the assumption that the emission from optically selected TDEs originates from X-ray photons from the accretion disc reprocessed by an optically thick quasi-spherical expanding outflow. Much like the cooling envelope model discussed in Section 5.1 this model is motivated by the 'low' blackbody temperature observed in optical TDEs, as well as their relatively low X-ray luminosities and late-time radio emission.

In their model, T. Matsumoto & T. Piran (2021) determine two radii defined by E. Nakar & R. Sari (2010) and R.-F. Shen et al. (2015). The first is the diffusion radius R_d, above which radiation can freely escape as the photons diffusion time is shorter than the dynamical time of the ejecta, defined at an optical depth of $\tau(R_d) = \frac{c}{v_d}$. The second is the colour radius, at which the photons are last considered to be in thermal equilibrium with the ejecta, defined at an optical depth of $\tau_{eff}(R_c) = 1$.

As input, the model takes the evolution of the transient's luminosity and temperature in order to determine the locations of these radii over time, as well as the outflow density ρ at these radii. These parameters also depend on the outflow velocity v, which is varied over a range of possible values as an additional input parameter. As stated by T. Matsumoto & T. Piran (2021), for TDEs with outflow velocities lower than the critical velocity v_c at which $R_d = R_c$, $R_c > R_d$. For AT2019cmw this critical velocity lies at $v > 10^4$ km s^{-1}. This is above the approximate upper limit of velocities in the reprocessing-outflow model that T. Matsumoto & T. Piran (2021) consider, which was set considering observations
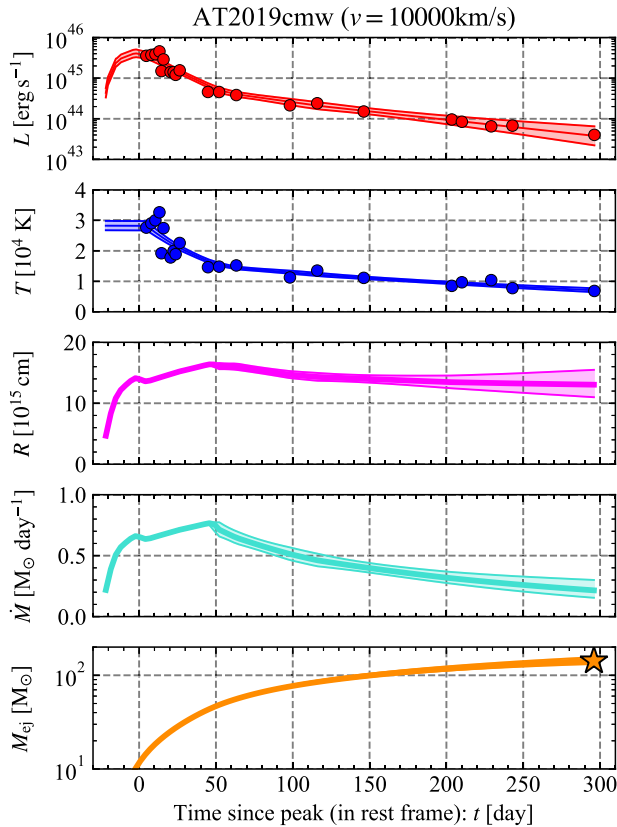
Figure 12. Input and derived output parameters for our fit of AT2019cmw to the reprocessing-outflow model from ~ 20 d pre-peak up to ~ 300 d post-peak. The curves and corresponding error regions plotted show the input luminosities and temperatures used in the model fit, as well as output colour radii, mass-ejection rate per day and cumulative ejecta mass over time. Data points show our derived blackbody characteristics of AT2019cmw from Section 3.2.

Figure 13. Predicted ejecta masses for AT2019cmw in the 'reprocessing-outflow' model for a range of assumed input ejecta velocities.

of TDEs that display broad emission features at a velocity of $v \lesssim 10^4 \mathrm{km\,s^{-1}}$ (I. Arcavi et al. 2014). As a result, the rate of mass ejection can be determined for this event using the equation $\dot{M}_c = 4\pi R_c^2 \rho_c v$.

We performed an initial fit to our derived blackbody luminosities and temperatures over the first 300 d in AT2019cmw's rest-frame. As can be seen in Fig. 12, for an outflow velocity of $v = 10^4 \mathrm{km\,s^{-1}}$ we find an ejecta mass of $\sim 142 \pm 10\,\mathrm{M_\odot}$ in the first 300 d post-peak luminosity. Fig. 13 shows the range of ejecta masses we estimate for a range of input outflow velocities.

Following the method from T. Matsumoto & T. Piran (2021), we consider the lower-limit on the outflow velocity in this model to be the escape velocity of the system, for which we use the following relation:

$$v_{esc}(R_c) \simeq 1900\ \mathrm{km\,s^{-1}} M_{BH,6.5}^{1/2} L_{44}^{-3/10} T_4^{17/20}. \qquad (3)$$

When applying our peak values for temperature and luminosity from Section 3.2, and the fiducial SMBH mass of $10^{6.5}\,\mathrm{M_\odot}$ used by T. Matsumoto & T. Piran (2021), we find an escape velocity at R_c of $v_{esc}(R_c) \sim 1.5 \times 10^3\ \mathrm{km\,s^{-1}}$. This corresponds to an ejected mass of $\sim 30\,\mathrm{M_\odot}$ when applied to Fig. 13. Even when applying our lower limit on the SMBH mass from Section 5.3 of $M_{bh} = 1 \times 10^5\,\mathrm{M_\odot}$, we find $v_{esc}(R_c) \sim 3 \times 10^2\ \mathrm{km\,s^{-1}}$, and thus $\sim 6\,\mathrm{M_\odot}$ of ejecta.

A significant caveat of this model is the assumption of quasi-spherical outflows with densities, temperatures and velocities that do not vary with viewing angle. T. Matsumoto & T. Piran (2021) state that if outflows in TDEs vary strongly with viewing angle, then their observed characteristics could be explained with a lower ejecta mass than calculated for the quasi-spherical case.

Nevertheless, the ejecta mass required to explain AT2019cmw's observed blackbody evolution in this model is ~ 8.5 times larger than the highest estimate for their sample at an ejecta velocity of $\sim 3 \times 10^2\ \mathrm{km\,s^{-1}}$. We note that this is below their approximate lower limit on the outflow velocity of $\sim 10^3\ \mathrm{km\,s^{-1}}$ for typical SMBHs. Whilst we lack concrete observational evidence of an outflow of the kind described by the reprocessing-outflow model, as we see continuously featureless spectra and a lack of detected late-time radio emission (as will be discussed in Section 7.5), this is evidence that a large amount of material may be needed to explain AT2019cmw's observed characteristics in the context of this model.

This, combined with the high disrupted star masses estimated by our REDBACK models in Sections 5.1 and 5.3, supports the interpretation that AT2019cmw may be the result of the tidal disruption of a high-mass star.

7 DISCUSSION

7.1 Disrupted star mass

We can infer a conservative minimum value of $\sim 0.9\,\mathrm{M_\odot}$ for the mass of the disrupted star using the integrated emitted energy post-peak found in Section 3.2, assuming an accretion efficiency of 10 per cent. However, although we note that our mass estimates are dependent on assumptions for values such as η, κ and the exact emission geometry of AT2019cmw, our model fits in Sections 5.1, 5.3, and 6 suggest that AT2019cmw is the result of the disruption of a star in the tens of solar masses. In these model fits, this interpretation is favoured to explain AT2019cmw's other observed features, such as its extreme peak luminosity and consistently large blackbody radius. As seen in equation (1) from N. Sarin & B. D. Metzger (2024), for example, the photospheric
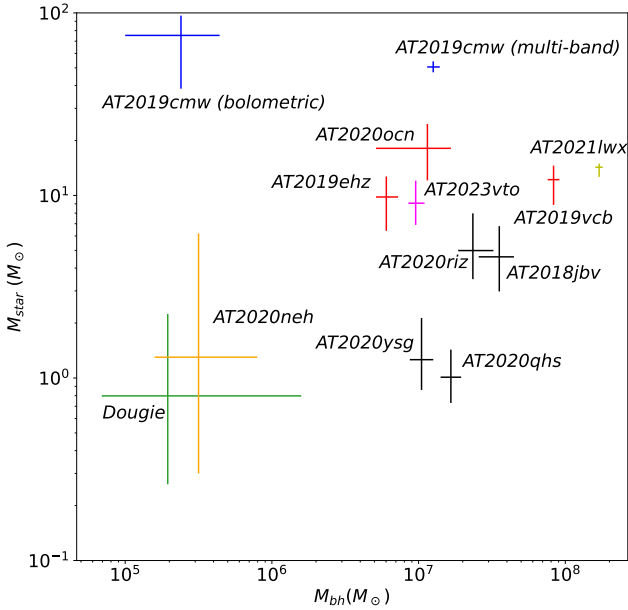
Figure 14. MBH and disrupted star masses from AT2019cmw's RED-
BACK model fits and literature TDEs. 95 per cent confidence intervals
for AT2019cmw as detailed in Sections 5.1 and 5.3 are displayed. Plotted
for comparison are AT2021lwx (B. M. Subrayan et al. 2023), AT2023vto
(H. Kumar et al. 2024), AT2020neh (C. R. Angus et al. 2022) and Dougie
(J. Vinkó et al. 2014). The featureless TDEs from E. Hammerstein et al.
(2023), as well as the events with the highest predicted disrupted star
masses from their TDE-H (AT2019ehz), TDE-He (AT2020ocn) and TDE-
H + He (AT2019vcb) subclass, are also displayed in black and red,
respectively.

radius in the model is proportional to the natural logarithm of
the envelope mass.

Fig. 14 shows the values from our model fits for AT2019cmw
from Sections 5.1 and 5.3 compared to a subsample of TDEs and
candidate TDEs with well-measured estimates of the masses of
the disrupted star and black hole from the literature. For com-
parison we chose the featureless TDEs from E. Hammerstein
et al. (2023) that appear spectroscopically similar to AT2019cmw,
as well as the events with the highest disrupted star masses es-
timated for each of their other three spectroscopic subclasses.
We also chose AT2023vto and AT2021lwx for comparison, recent
well-studied events with notably high estimates for the mass
of the disrupted star. Additionally, we show AT2020neh (C. R.
Angus et al. 2022) and Dougie (J. Vinkó et al. 2014), events
that appear to show significant post-peak cooling, similar to
AT2019cmw. Dougie also displays featureless spectra throughout
its evolution.

As can be seen in Fig. 14, the disrupted star masses for
AT2019cmw that we infer from our model fits are significantly
different from those found by E. Hammerstein et al. (2023) for
the featureless TDEs in their sample fit to the model from B.
Mockler et al. (2019) using MOSFiT (J. Guillochon et al. 2018).
The events from E. Hammerstein et al. (2023) all converge to a
disrupted star mass of $M_* < 10\,M_\odot$ despite being a similar peak
luminosity to AT2019cmw. They do however find that TDE-He
events converge on average to a high disrupted star mass, with
2 out of 3 of their TDE-He events converging to a stellar mass
of 10-20 $M_\odot$ in MOSFiT. They state that this is possibly because

they result from the disruption of evolved high mass stars. They
also find three TDE H + He events that converge to disrupted
star masses of $\gtrsim 10\,M_\odot$ in MOSFiT. The event AT2019ehz in their
sample also converged to a mass of $\sim 10M_\odot$ in MOSFiT despite
being a TDE-H event.

Another example is AT2021lwx, which is hypothesized by B.
M. Subrayan et al. (2023) to be a TDE of a $\sim 14\,M_\odot$ star. It was
also categorized as an ENT by J. T. Hinkle et al. (2025), which
they hypothesise are TDEs of 3-10 $M_\odot$ stars. However, as noted
by P. Wiseman et al. (2023), in which they explore a non-TDE
interpretation of AT2021lwx, the event displays AGN-like emis-
sion features. They find that it shows broad Balmer emission,
as well as emission features from magnesium, helium and car-
bon, distinct from events in the TDE subclasses defined by S.
Velzen et al. (2021). As we state in Section 4.2, J. T. Hinkle et al.
(2025) hypothesise that the Mg II emission seen in ENTs such as
Gaia18cdj, shown in Fig. 4 for comparison, could be the result
of a pre-existing gas reservoir in close proximity to the SMBH. It
is possible that the interaction of the stellar debris from a TDE
with such a pre-existing gas reservoir could provide an additional
source of luminosity, thus increasing the apparent disrupted star
mass required to power the flare, but it is currently unknown
whether this is the case for ENTs.

In the case of AT2019cmw, it is observationally a featureless
event yet still has a high estimated disrupted star mass. Although,
any emission lines may be too weak and/or broadened to be
detected. Combined with the events discussed above, it is addi-
tional evidence that a variety of spectral appearances may result
from TDEs of high mass stars, perhaps due to variations in the
evolutionary stages of the disrupted stars or environment around
the disrupting SMBH. In the case of the TDE-He events from
E. Hammerstein et al. (2023) and AT2023vto from H. Kumar
et al. (2024), which show helium in emission alongside a lack
of hydrogen, it is possible that the stars were stripped of their
hydrogen envelopes prior to disruption. If this was a result of
the stars having ejected their outer layers after leaving the main
sequence, as is the case for Wolf-Rayet stars (G. Meynet & A.
Maeder 2003), spectral signatures of heavier elements such as
carbon, nitrogen and oxygen may be visible at other wavelengths
such as the rest-frame UV. However, as a high mass star would
spend a much smaller proportion of its lifetime off of the main
sequence than on it, the likelihood of this being the case at the
time of disruption is small.

7.1.1 Implications of a high mass star disruption

The disruption of a star in the tens of solar masses by a SMBH
would imply that there is ongoing massive star formation close
to the SMBH in AT2019cmw's host, as these stars have lifetimes
of only a few million years or less (S. Ekström et al. 2012) and
so have a very limited time in which to be disrupted by the black
hole. AT2019cmw's host appears to be red and poorly star form-
ing, so this raises questions about how the immediate vicinity of
its SMBH differs from the surrounding galaxy. If our estimate
of the disrupted star mass is correct, it suggests that accreted
intergalactic gas, or perhaps an accreted dwarf galaxy, could have
caused a small region of massive star formation in the environ-
ment close to the SMBH. For instance, the formation of massive
stars has been observed at the heart of our own Galaxy, with
dozens of young massive star candidates found within the central

2.5 parsecs of the galactic centre by S. Nishiyama & R. Schödel (2013). Smoothed particle hydrodynamic simulations from I. A. Bonnell & W. K. M. Rice (2008) have also showed that star formation from gas infalling into the environment around the SMBH can produce a population with a top-heavy IMF.

Evidence of active massive star formation in early-type galaxies may have been seen in the case of SN2006gy (E. O. Ofek et al. 2007; N. Smith et al. 2007). The recent study from A. Jerkstrand, K. Maeda & K. S. Kawabata (2020) for instance suggests that a common envelope ejection from the merger of a white dwarf and a massive hydrogen-rich star shortly before a Type Ia supernova could explain its extreme luminosity. Centrally concentrated star formation has also been observed in NGC 3182 (M. Pak et al. 2023), as well as a centrally concentrated molecular outflow in NGC 1266 (K. Alatalo et al. 2011), both of which are nearby early-type lenticular galaxies. However, it should be noted that for NGC 3182 and NGC 1266 these phenomena are associated with AGN-driven outflows (K. Alatalo et al. 2015; M. Pak et al. 2023), whereas we do not see evidence of an AGN in AT2019cmw's host.

7.2 Black hole mass

As can be seen in Fig. 14, we find values of $M_{\rm bh}$ separated by almost two orders of magnitude from our REDBACK cooling envelope model fits from Sections 5.1 and 5.3, at $M_{\rm bh} \approx 1.3 \times 10^7 M_\odot$ and $M_{\rm bh} \approx 2.4 \times 10^5 M_\odot$ respectively. As we discuss in Section 5.3, combined with the discrepancy between our estimates of $M_{\rm bh}$ and the independent high values of $M_{\rm bh}$ found by Y. Yao et al. (2023) and A. Mummery et al. (2024) for AT2019cmw, this suggests that at later times the cooling envelope may not accurately describe AT2019cmw's evolution. Although it appears that a high disrupted star mass may be required to explain our near-peak observations, as it evolves AT2019cmw may deviate significantly from the physical assumptions in current TDE models.

Expanding our comparison to other similar events, such as the featureless TDEs found by E. Hammerstein et al. (2023), (Y. Yao et al. 2022) as well as the events in the sample by Y. Yao et al. (2023) (E. Hammerstein et al. 2021; M. Chu, A. Dahiwale & C. Fremling 2022), we find that these events are generally predicted to have high black hole masses. E. Hammerstein et al. (2023) note that their host galaxies are significantly larger than those of other TDE subclasses in their sample, with their MOSFiT fits outputting significantly larger black hole masses. However, some events go against this trend. For example, the candidate featureless TDE Dougie (J. Vinkó et al. 2014) appears to have a disrupting black hole mass of $M_{bh} = 1.95^{+13.90}_{-1.26} \times 10^5 M_\odot$ from TDEFiT modelling (J. Guillochon, H. Manukian & E. Ramirez-Ruiz 2014), which is potential evidence against this being the case for all of these events. A high black hole mass also doesn't appear to always result in a featureless event. As can be seen in Fig. 14, the TDE-H + He AT2019vcb from E. Hammerstein et al. (2023) has a higher value of M_{bh} from MOSFiT than all featureless TDEs in their sample. AT2021lwx, which B. M. Subrayan et al. (2023) find is a TDE from a black hole with $M_{bh} = 1.7 \pm 0.1 \times 10^8 M_\odot$, and hypothesized by J. T. Hinkle et al. (2025) to be a TDE around a high mass ($> 10^8 M_\odot$) black hole, has a higher black hole mass than all events from E. Hammerstein et al. (2023). Due to the diversity of derived black hole masses found for TDEs of various spectral classes, whether there is a physical link between the mass of the disrupting black hole and the spectral appearance of the resulting TDE is currently uncertain.

One possible reason for the diversity of derived black hole masses is systematic model differences. A comparison between values of M_{bh} for 5 TDEs derived using MOSFiT by E. Hammerstein et al. (2023), TDEMASS by T. Ryu, J. Krolik & T. Piran (2020) and the cooling envelope model in REDBACK is presented in table 4 of N. Sarin & B. D. Metzger (2024). For 4 of these events, the predicted values are consistent to within an order of magnitude. However, for the faint and fast event AT2020wey I. Arcavi et al. (2020), P. Charalampopoulos et al. (2023) and E. Hammerstein et al. (2023) find a value of M_{bh} approximately 2 orders of magnitude greater than T. Ryu et al. (2020) and N. Sarin & B. D. Metzger (2024).

Although AT2019cmw was found to have a high black hole mass by Y. Yao et al. (2023) and A. Mummery et al. (2024), the discrepancy between the values of M_{bh} we find from our cooling envelope model fits means that we cannot confirm whether it actually was the result of a TDE from a high mass SMBH. The case of AT2020wey presented by N. Sarin & B. D. Metzger (2024) suggests that for events at the extreme ends of the TDE luminosity distribution, such as AT2019cmw, our current models may not be able to accurately measure their black hole masses, and that further theoretical work is needed.

7.3 Photometric comparison to other TDEs

In Fig. 14, we compare AT2019cmw to AT2021lwx (B. M. Subrayan et al. 2023; J. T. Hinkle et al. 2025) and AT2023vto (H. Kumar et al. 2024), two other well-studied TDEs with high disrupted star mass estimates. AT2019cmw's peak luminosity of $\log(L/{\rm ergs}^{-1}) \sim 45.6$ that we measure in Section 3.2 is comparable to the luminosity of $\log(L/{\rm ergs}^{-1}) = 45.7$ for AT2021lwx (B. M. Subrayan et al. 2023), and is significantly higher than AT2023vto's value of $\log(L/{\rm ergs}^{-1}) = 44.89^{+0.02}_{-0.03}$ as measured by H. Kumar et al. (2024). AT2019cmw's peak temperature of T = $10^{4.45}$ K is higher than the temperature of T = $10^{4.30}$ K measured by H. Kumar et al. (2024) for AT2023vto using spectral blackbody fitting, however they note that this is a conservative lower limit. AT2021lwx's peak temperature of T $\approx 10^{4.20}$K is somewhat lower than both. In terms of integrated radiated energy over their observed evolution, AT2019cmw and AT2023vto emit similar energies of $\sim 1.7 \times 10^{52}$ erg and $\sim 1.8 \times 10^{52}$ erg ,respectively. AT2021lwx was measured by B. M. Subrayan et al. (2023) to have radiated $\sim 9.7 \times 10^{52}$ erg, a much higher total radiated energy than AT2019cmw. Although this could suggest a higher disrupted star mass, it could also be indicative of a higher accretion efficiency. It could also be due to shocks from collisions between stellar debris and pre-existing material around the SMBH, as was already discussed in Section 7.1.

In Fig. 14, we also show AT2019ehz, AT2020ocn and AT2019vcb, the events from the TDE-H, TDE-He and TDE-H + He subclasses respectively with the highest estimated disrupted star masses in the sample from E. Hammerstein et al. (2023). Notably, even though these events have higher estimates for the mass of the disrupted star than the featureless TDEs (excluding AT2019cmw) they are less luminous at peak, with peak bolometric luminosities between $\log(L/{\rm ergs}^{-1}) \sim 43.6$ and $\log(L/{\rm ergs}^{-1}) \sim 44.0$. This is potential evidence that that a high disrupted star mass is not what is primarily driving featureless TDEs such as AT2019cmw to display such high luminosities, with other factors such as higher accretion efficiency possibly being more important. AT2019ehz and AT2019vcb are also cooler at
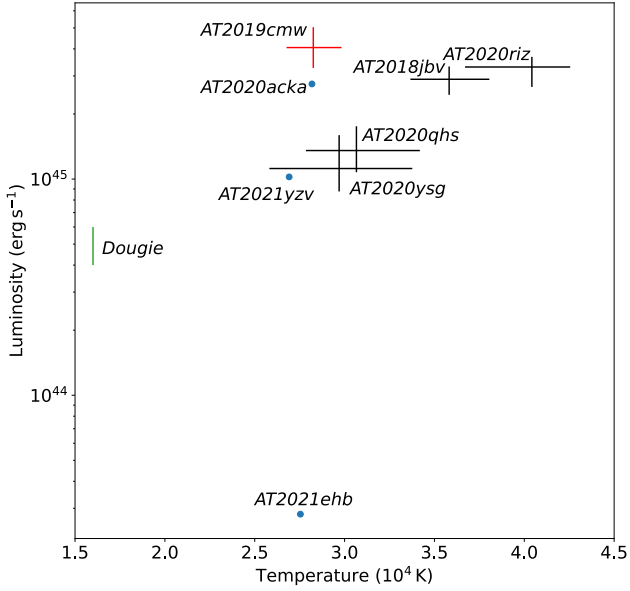
Figure 15. Temperatures and luminosities at peak of AT2019cmw and featureless TDEs from the literature. The featureless TDEs from E. Hammerstein et al. (2023) are shown in black, and the 3 featureless events from Y. Yao et al. (2023) are shown in red. The latter 3 events did not have associated uncertainties for their peak temperatures and luminosities. Dougie (J. Vinkó et al. 2014), shown in green, also did not have an uncertainty listed for its peak temperature.

peak than AT2019cmw and the featureless TDEs from E. Hammerstein et al. (2023), at $\sim 10^{4.3}$ and $\sim 10^{4.4}$ K, respectively. However AT2020ocn has a comparable peak temperature to the featureless TDEs at $\sim 10^{4.5}$ K. The case of AT2020ocn shows that featureless spectra may not be a temperature dependent phenomenon.

Whilst AT2019cmw has a peak temperature and luminosity similar to the featureless TDEs found by E. Hammerstein et al. (2023), as can be seen in Fig. 5, it seems to have evolved differently after peak. Its prompt cooling in the first 300 d post-peak is in contrast to their lack thereof, as they appear to stay at a constant temperature between $\sim 10^{4.4}$ and $\sim 10^{4.6}$ K. The evolution of AT2019cmw's inferred radius is also unlike other TDEs in this class, as they all display a decrease in their radius over time whereas it does not. In the case of its fading, it appears to be primarily driven by cooling rather than a decrease in its radius as previously seen in most other TDEs.

As seen in Fig. 15, expanding our comparison with other featureless TDEs paints a broader picture. The sample from Y. Yao et al. (2023) contains three additional featureless TDEs not included in E. Hammerstein et al. (2023)'s sample. Of these, AT2020acka (E. Hammerstein et al. 2021) and AT2021yzv (M. Chu et al. 2022), have comparable peak luminosities to those just discussed at $\log(L/\mathrm{erg\,s^{-1}}) = 45.44$ and $\log(L/\mathrm{erg\,s^{-1}}) = 45.01$ respectively. AT2021ehb (Y. Yao et al. 2022) however has a peak luminosity of $\log(L/\mathrm{erg\,s^{-1}}) = 43.54$. As stated by Y. Yao et al. (2022), this is evidence that featureless TDEs are not exclusively overluminous, such as in E. Hammerstein et al. (2023)'s sample. Although AT2019cmw is likely another example of an extremely luminous featureless TDE, the rarity of this subclass means that there is a selection bias towards finding more luminous events at high redshift.

Other events also hint at additional possible photometric diversity in this subclass. Y. Yao et al. (2023) for example finds TDEs from a wide variety of spectral classes with post-peak temperature change, with 11 TDEs in their sample showing significant $uvw2 - r$ colour evolution. Another example is AT2020neh (C. R. Angus et al. 2022), a fast-evolving TDE with broad hydrogen emission that displays significant post-peak temperature evolution. These events suggest that AT2019cmw's featureless spectral appearance and its atypical blackbody temperature evolution are likely two distinct and unrelated phenomena.

Dougie (J. Vinkó et al. 2014) is an example of an unclassified event that shows similarities to AT2019cmw and the featureless TDEs discussed above. It displayed a featureless continuum throughout its entire visible evolution, with only narrow host features visible at late times. Additionally, Dougie also cooled from ~ 13 kK to ~ 6.3 kK from 10 to 36 d post-peak, similar to the cooling seen in AT2019cmw and AT2020neh (C. R. Angus et al. 2022). However, it was significantly less luminous at peak than AT2019cmw and the featureless TDEs from E. Hammerstein et al. (2023), with $L_{\mathrm{peak}} = 5 \pm 1 \times 10^{44}\,\mathrm{erg\,s^{-1}}$. It was also somewhat cooler than other featureless TDEs at peak at ≈ 16 kK. Notably, J. Vinkó et al. (2014) found that Dougie was offset from its host nucleus by ~ 1.3 arcsec, which they state corresponds to ~ 3.9 kpc. This is in contrast to the nuclear locations of most other TDEs in the literature.

7.3.1 Luminous fast coolers as TDEs?

Dougie (J. Vinkó et al. 2014) has been speculated to be part of a possible new class of rapidly evolving transients, termed 'luminous fast coolers' (LFCs) by M. Nicholl et al. (2023), with AT2022aedm and AT2020bot (A. Y. Q. Ho et al. 2023) also presented as possible members of this class. These events appear to display many similarities to AT2019cmw. AT2022aedm for instance reaches a peak luminosity of $\sim 10^{45}\,\mathrm{erg\,s^{-1}}$ and displays spectra lacking broad emission features throughout its observed evolution. Notably, it cools post-peak from ~ 30 kK to ~ 4 kK whilst appearing to show an expanding rather than contracting photosphere, and displays no significantly detected X-ray or radio emission, with Dougie also being undetected in X-ray (J. Vinkó et al. 2014). All three events also occurred in hosts with low SFRs.

However, as stated by M. Nicholl et al. (2023), these events are all significantly offset from their host galaxies' nuclei. M. Nicholl et al. (2023) also show that AT2022aedm's spectra are not entirely featureless, displaying narrow emission features at early times and narrow absorption at late times, with A. Y. Q. Ho et al. (2023) also finding that AT2020bot displays unidentified broad spectral features.

Although some characteristics of LFCs are in contrast to what we find for AT2019cmw, their similarities are still notable. M. Nicholl et al. (2023) speculate that LFCs may be caused by TDEs from intermediate or stellar-mass black holes due to their fast evolution and non-nuclear locations in their hosts. As a result, AT2019cmw may be related to this class of events, possibly representing a 'missing link' between LFCs and previously classified TDEs. This, and the colour-changing TDEs discussed in Section 7.3, suggest that there may be extensive photometric in addition to spectral heterogeneity in TDEs. However, the physical mechanism that causes some TDEs to significantly redden in contrast to most other classified events is currently unknown.

Due to their post-peak colour evolution and often ambiguous spectra, it is possible that other featureless and/or cool-

ing AT2019cmw-like TDEs/LFCs may have gone unclassified, or were misclassified as other classes of transients. AT2020bot, for example, was noted to have unidentified broad spectral features similar to Type Ic-BL SNe by A. Y. Q. Ho et al. (2023). A larger sample of well-studied events is required to better determine the observational similarities and differences between these subclasses. The ability to accurately distinguish between them photometrically will be essential to uncovering their driving mechanisms, especially with the large number of expected TDE discoveries from the upcoming Vera C. Rubin observatory (Z. Ivezić et al. 2019; K. Bricman & A. Gomboc 2020).

7.4 Deviations from simple blackbody evolution in the UV

As described in Section 3.3, AT2019cmw's *u*-*g* colour increases at a high rate shortly after peak before slowing. For a simple cooling blackbody, one would expect the rate of reddening in $u - g$ to increase rather than decrease as the peak wavelength of the blackbody emission increases past the *u*-band, and the *u*-band increasingly samples the Wien tail of a cooling black body. One possibility is that we are observing emission from inhomogeneous regions of material surrounding the black hole with different temperatures, rather than one homogeneous region with a single temperature. As we state in Section 3.2.1, this possibility motivated us to attempt a multi-component blackbody fit to explain the potential underluminosity we see in the *Swift* UV bands compared with the optical. This did not result in an improvement in our fits.

J. Vinkó et al. (2014) also observed a UV underluminosity in Dougie, similar to what we observe for AT2019cmw in Section 3.2.1. One possible explanation that they suggested was the appearance of UV absorption features as seen in the case of PS1-11af by R. Chornock et al. (2013). As seen in Fig. 4, the spectra that we obtained from LRIS cover a large portion of the same wavelengths as the *u*-band filter on the LT (1950 Å to 2632 Å in rest-frame), and do not show any emerging absorption features. As such, this likely does not explain the rapid *u*-band fading that we observe from AT2019cmw. The physical origin of this behaviour is therefore currently unknown.

However, the presence of UV absorption features at wavelengths not covered by our optical spectroscopy could potentially explain an underluminosity in the *Swift* UV bands that we find hints of in Fig. 6. As can be seen in fig. 9 of T. Hung et al. (2019), several TDEs display prominent UV spectral features, both in absorption and emission between $\sim$ 1000-2000 Å. A notable example that they show is the TDE iPTF15af which, although its optical spectra presented with hydrogen and helium emission features superimposed on a blue continuum in contrast to AT2019cmw's featureless spectra, showed broad UV absorption troughs from elements such as oxygen and carbon similar to broad absorption line quasars (N. Blagorodnova et al. 2019). Comprehensive UV spectral follow-up of a larger sample of TDEs would be useful in determining how common such UV spectral features are in TDEs.

Potential UV absorption features are not taken into account in the model fits discussed in Sections 5.1 and 6, although our RED-BACK model fit suggested significant host extinction/reddening. The presence of any UV absorption features could mean that our value for host extinction, and thus our estimate for the luminosity and disrupted star mass, are overestimated. As stated in Section 5.2 however, when we performed a fit to the Cooling Envelope model using our derived blackbody luminosities from

Section 3.2 that neglect any internal extinction or UV suppression, we still predict a high disrupted star mass. As our fit to the reprocessing-outflow model in Section 6 was also performed using these same luminosities, we can conclude that any UV suppression that may be present is not significantly affecting our estimates of the disrupted star mass.

7.5 Observational evidence of jets and outflows

Several TDEs have been observed at extreme luminosities in the radio. *Swift* J164449.3+573451 (Y. Cendes et al. 2021) for example appears to show bright emission from on-axis jets, with its radio luminosity exceeding 10^{40} erg s^{-1} for over 1000 d post-first detection (Y. Cendes et al. 2024), $\sim$ 2 order of magnitude greater than our upper limit of $\nu L_\nu = 2.8 \times 10^{38}$ erg s^{-1} for AT2019cmw from Section 3.5. Another event that Y. Cendes et al. (2024) discuss is AT2022cmc (I. Andreoni et al. 2022), which has a radio luminosity evolution so far very similar to Swift J164449.3+573451 and is thought to also possess an on-axis jet. Optically, AT2022cmc is a useful comparison event in this context, as I. Andreoni et al. (2022) and E. Hammerstein et al. (2025) note that after its initial fast-fading red light-curve it displays a blue, optically luminous plateau with featureless spectra. They suggest a possible link between TDEs with relativistic jets and the featureless TDEs from the sample by E. Hammerstein et al. (2023). Just as we do not see evidence in the radio, we do not see evidence of jetted optical emission for AT2019cmw as was the case for AT2022cmc. However, this only provides evidence against the presence of on-axis jetted emission in AT2019cmw, as an off-axis jet at a large viewing angle would not display the same observational characteristics as shown by AT2022cmc.

I. Andreoni et al. (2022) state in their study of AT2022cmc that when correcting for beaming effects, the rate that they calculate for on-axis relativistic TDEs means that $\sim$ 1 per cent of TDEs produce relativistic jets. However, Y. Cendes et al. (2024) observed 23 optically selected TDEs, and detected 10 with radio emission (that did not come from star formation in the host or a pre-existing AGN) with luminosities ranging from 10^{37} 10^{39} erg s^{-1}. They state that their observations are at odds with off-axis relativistic jets being able to explain this population of TDEs, and suggest that the emission instead may be explained by a non-relativistic outflow from processes such as late-time disc formation. As can be seen in fig. 1 of Y. Cendes et al. (2024), some events in their sample are detected at luminosities an order of magnitude fainter than our upper limit for AT2019cmw at similar times. As such, our upper limit is relatively non-constraining in this context. However, some events in their sample such as ASASSN-14ae (T. W. S. Holoien et al. 2014; J. L. Prieto et al. 2014) and AT2018hyz (I. Arcavi 2018; Y. Cendes et al. 2022) were detected at much later times than our observations, with their luminosities continuing to rise over time. ASASSN-14ae for instance was first detected in radio 2313 days post-optical discovery by Y. Cendes et al. (2024), with its luminosity increasing to $\sim 10^{38}$ erg s^{-1} 930 d later, which is approaching our upper limit for AT2019cmw.

Although we place tight constraints on the presence of an on-axis jetted component for AT2019cmw, one that is significantly off-axis cannot be ruled out. We also cannot discount that there was radio emission present from a non-relativistic late-launched outflow below our detection limit, or that it may become significantly detectable at later times. As such, continued late-time radio monitoring of AT2019cmw and other similar events is warranted.

8 CONCLUSIONS

We have presented a comprehensive analysis of the extraordinary spectroscopically featureless nuclear transient AT2019cmw. Following an intense photometric and spectroscopic follow-up campaign, we found it to have a peak luminosity of $L_{\text{peak}} \sim 10^{45.6}\,\text{erg s}^{-1}$ from blackbody SED fitting, making it one of the most luminous thermal transients ever discovered. Its post-peak photometric evolution is peculiar when compared with most other TDEs. Additionally, our model fits to its photometry and luminosity evolution imply the involvement of a massive star in close proximity to its host's SMBH.

(i) Although AT2019cmw's relatively fast rise, extreme luminosity and post-peak cooling could theoretically be explained with the scenario of a highly superluminous supernova, the combination of its lack of visible spectral features throughout its evolution as well as its blackbody temperature and radius evolution make it difficult to explain in this context. The host galaxy's SED from Y. Yao et al. (2023), the lack of any detected AGN spectral lines and the absence of significant detected activity attributable to an AGN in forced photometry also suggests that it is unlikely that there is a preexisting AGN in the host. This, alongside its blue colour at peak and $t^{-5/3}$ power-law luminosity decline post-peak, is consistent with AT2019cmw being a peculiar featureless TDE.

(ii) Our cooling envelope model fits in Sections 5.1 and 5.3 converge to SMBH masses that deviate by ~ 2 orders of magnitude. As we state in Section 7.2, this implies that the physical assumptions in current TDE models are not sufficient to explain the photometric evolution of AT2019cmw, especially at later times. This is also highlighted by our difficulty in reproducing AT2019cmw's post-peak colour evolution in our fit of its multiband photometry in Section 5.1. Alongside the previously noted systematic differences between parameters estimated by different TDE models for the extreme event AT2020wey (N. Sarin & B. D. Metzger 2024), this suggests that additional theoretical work is needed to improve current TDE models.

(iii) We determine a conservative lower-limit of $\sim 0.9\,\text{M}_\odot$ for the mass of the disrupted star from a measured radiated energy of $\sim 1.7 \times 10^{52}$ erg. However, our photometric fits using both the 'cooling envelope' and 'reprocessing-outflow' models suggest that AT2019cmw was the result of the disruption of a $> 10\,\text{M}_\odot$ star. Although our models may be somewhat overestimating the mass of the disrupted star when compared to reality its physical characteristics, such as its consistently large blackbody radius, suggest that a high mass star is likely required to explain our observations of AT2019cmw. A TDE of a high mass star suggests that although AT2019cmw's host is broadly poorly star forming, it may possess a region of active star formation close to its SMBH, potentially due to accreted intergalactic gas. Our high estimate for AT2019cmw's disrupted star mass, in addition to the potential TDEs of high mass stars from E. Hammerstein et al. (2023), J. T. Hinkle et al. (2025), and P. Wiseman et al. (2025), could point to a top-heavy IMF in close proximity to some SMBHs, as suggested by the simulations from I. A. Bonnell & W. K. M. Rice (2008).

(iv) AT2019cmw's SED shows a transient near-UV underluminosity shortly post-peak, as was seen in the candidate-TDE Dougie (J. Vinkó et al. 2014). It also appears to show $u - g$ reddening at a faster rate than is expected for a simple cooling blackbody. The physical origins of these behaviours are currently unknown. This points to the need for comprehensive UV photometric follow-up of similar events, as well as UV spectroscopic follow-up, in order to probe for deviations from a simple blackbody SED and/or the presence of absorption features in the UV.

(v) Our radio upper-limit of $\nu L_\nu < 2.8 \times 10^{38}\,\text{erg s}^{-1}$ at 971 d post-peak in rest frame, as well as the lack of an initial red, fast-fading phase of its optical light-curve as was seen in the case of AT2022cmc (I. Andreoni et al. 2022), places tight constraints on the presence of any early on-axis relativistic jetted emission from AT2019cmw. However, observations from Y. Cendes et al. (2024) suggest that some TDEs can first display rising radio emission thousands of days post-first optical detection, possibly from non-relativistic outflows. This points to the need for continuing deep radio follow-up of AT2019cmw and other similar events in order to search for evidence of late-launched outflows that may become visible at later times.

(vi) Our *Swift* XRT X-ray upper limit of $\gtrsim 3 \times 10^{43}$ erg s^{-1}, observed between ~ 12 and ~ 54 d post-peak in AT2019cmw's rest-frame, is not particularly constraining on the presence of X-ray emission. However, the ratio between AT2019cmw's derived blackbody luminosity and its X-ray luminosity ($L_{\text{BB}}/L_{\text{X}}$) upper limit was ~ 50-100. In comparison, 6 out of 8 of the X-ray detected TDEs observed in the sample from E. Hammerstein et al. (2023) at a similar time post-peak showed $L_{\text{BB}}/L_{\text{X}} \lesssim 50$. This implies that AT2019cmw was not an X-ray luminous event at the time of our observations.

(vii) Alongside other similar events, its atypical post-peak blackbody temperature and radius evolution possibly points to the presence of significant photometric heterogeneity in the TDE landscape. AT2019cmw possibly represents a 'missing link' between TDEs and the recently categorized LFCs, which M. Nicholl et al. (2023) speculate may be peculiar TDEs from IMBHs or stellar mass black holes.

We have found AT2019cmw to be an extreme event in many aspects, with few analogous events in the literature. Our model estimates of a high disrupted star mass, if correct, point to the possibility that TDEs could provide a unique window from which we could probe star formation in close proximity to their host galaxies' SMBH. However, our REDBACK fits have highlighted the difficulties in measuring SMBH masses by fitting light-curves using current TDE models, suggesting that additional theoretical work is currently needed to improve their physical accuracy. Many of the driving mechanisms behind aspects of AT2019cmw's and other atypical TDEs' evolution are also currently unknown, such as what causes the presentation of featureless spectra, and why some TDEs appear to cool post-peak whilst others do not. With >35000 new TDE discoveries expected from the Vera C. Rubin observatory (Z. Ivezić et al. 2019; K. Bricman & A. Gomboc 2020), and observatories such as the La Silla Schmidt Southern Survey (LS4; A. A. Miller et al. 2025) due to begin science operations in the near future, many more AT2019cmw-like events will soon be discovered. Significantly increasing our sample size of well-studied edge cases such as AT2019cmw will allow us to probe the limits of current TDE models. It will also allow us to better study the observational similarities and differences between peculiar and 'normal' TDEs, improving our understanding of both sub-populations, as well as enabling us to refine our photometric filtering methods when separating TDEs and supernovae.

DATA AVAILABILITY

The data presented in this paper will be provided upon request to the author. Spectra are available to download on WISeREP. Photometry is listed in online supplementary data tables.

REFERENCES

Aghanim N. et al., 2020, A&A, 641, A6
Alatalo K. et al., 2011, ApJ, 735, 88
Alatalo K. et al., 2015, ApJ, 798, 31
Andalman Z. L., Liska M. T. P., Tchekhovskoy A., Coughlin E. R., Stone N., 2022, MNRAS, 510, 1627
Andreoni I. et al., 2022, Nature, 612, 430
Angus C. R. et al., 2022, Nat. Astron., 6, 1452
Arcavi I., 2018, Transient Name Server Classification Report, 2018-1764, 1
Arcavi I. et al., 2014, ApJ, 793, 38
Arcavi I., Burke J., Nyiha I., Howell A., Hiramatsu D., McCully C., Pellegrino C., Gonzalez E. P., 2020, Transient Name Server Classification Report, 2020-3228, 1
Ashton G. et al., 2019, ApJS, 241, 27
Barbary K., 2016, J. Open Source Softw., 1, 58
Bellm E., Kulkarni S., 2017, Nat. Astron., 1, 1
Bellm E. C. et al., 2019, PASP, 131, 018002
Bertin E., 2013, Astrophysics Source Code Library, record ascl: 1301.001
Bertin E., Arnouts S., 1996, A&AS, 117, 393
Bertin E., Mellier Y., Radovich M., Missonnier G., Didelon P., Morin B., in 2002,Bohlender D. A., Durand D., Handley T. A., eds, ASP Conf. Proc. Vol. 281, Astronomical Data Analysis Software and Systems XI. Astron. Soc. Pac., San Francisco, p. 228
Bida T. A., Dunham E. W., Massey P., Roe H. G., 2014, in Proc. SPIE Conf. Ser. Vol. 9147, Gound-based and Airborne Instrumentation for Astronomy. SPIE, Bellingham, p. 940
Blackburn J. K., Shaw R. A., Payne H. E., Hayes J. J. E., Heasarc, 1999, Astrophysics Source Code Library, record ascl:9912.002
Blagorodnova N. et al., 2018, PASP, 130, 035003
Blagorodnova N. et al., 2019, ApJ, 873, 92
Bloom J. S. et al., 2011, Science, 333, 203

Bonnell I. A., Rice W. K. M., 2008, Science, 321, 1060
Bricman K., Gomboc A., 2020, ApJ, 890, 73
Buitinck L. et al., 2013, preprint (arXiv:1309.0238)
Burrows D. N. et al., 2005, Space Sci. Rev., 120, 165
Cendes Y., Eftekhari T., Berger E., Polisensky E., 2021, ApJ, 908, 125
Cendes Y. et al., 2022, ApJ, 938, 28
Cendes Y. et al., 2024, ApJ, 971, 185
Chambers K. C. et al., 2016, preprint(arXiv:1612.05560)
Charalampopoulos P., Pursiainen M., Leloudas G., Arcavi I., Newsome M., Schulze S., Burke J., Nicholl M., 2023, A&A, 673, A95
Chen Z. H. et al., 2023, ApJ, 943, 41
Chornock R. et al., 2013, ApJ, 780, 44
Chrimes A. A. et al., 2024, MNRAS, 527, L47
Chu M., Dahiwale A., Fremling C., 2022, Transient Name Server Classification Report, 2022-363, 1
Cleveland W. S., 1979, J. Am. Stat. Assoc., 74, 829
Cleveland W. S., 1981, Am. Stat., 35, 54
Code A. D., Davis J., Bless R. C., Brown R. H., 1976, ApJ, 203, 417
Coughlin M. W. et al., 2023, ApJS, 267, 31
Dekany R. et al., 2020, PASP, 132, 038001
Djorgovski S. G. et al., 2011, preprint (arXiv:1102.5004)
Dong S. et al., 2016, Science, 351, 257
Drake A. J. et al., 2009, ApJ, 696, 870
Drout M. R. et al., 2014, ApJ, 794, 23
DuPuy D., Schmitt J., McClure R., van den Bergh S., Racine R., 1969, ApJ, 156, L135
Ekström S. et al., 2012, A&A, 537, A146
Fiorucci M., Ciprini S., Tosti G., 2004, A&A, 419, 25
Flewelling H. A. et al., 2020, ApJS, 251, 7
Foreman-Mackey D., 2016, J. Open Source Softw., 1, 24
Fremling C. et al., 2016, A&A, 593, A68
Fremling C. et al., 2020, ApJ, 895, 32
Gal-Yam A., 2019, ARA&A, 57, 305
Gal-Yam A., Maoz D., Guhathakurta P., Filippenko A. V., 2008, ApJ, 680, 550
Gehrels N. et al., 2004, ApJ, 611, 1005
Gezari S., 2021, ARA&A, 59, 21
Ghisellini G., Tavecchio F., Foschini L., Ghirlanda G., 2011, MNRAS, 414, 2674
Goldoni P. et al., 2021, A&A, 650, A106
Graham M. J. et al., 2019, PASP, 131, 078001
Grotova I. et al., 2025, A&A, 697, A159
Guillochon J., Ramirez-Ruiz E., 2013, ApJ, 767, 25
Guillochon J., Manukian H., Ramirez-Ruiz E., 2014, ApJ, 783, 23
Guillochon J., Nicholl M., Villar V. A., Mockler B., Narayan G., Mandel K. S., Berger E., Williams P. K. G., 2018, ApJS, 236, 6
HI4PI Collaboration et al., 2016, A&A, 594, A116
Hajela A. et al., 2025, ApJ, 983, 29
Hammerstein E. et al., 2021, Transient Name Server Classification Report, 2021-262, 1
Hammerstein E. et al., 2023, ApJ, 942, 9
Hammerstein E. et al., 2025, ApJ, 996, 143
Hart K. et al., 2023, preprint (arXiv:2304.03791)
Hills J. G., 1975, Nature, 254, 295
Hinkle J. T. et al., 2025, Sci. Adv., 11, eadt0074
Ho A. Y. Q. et al., 2023, ApJ, 949, 120
Ho A. Y. Q. et al., 2025, ApJ, 989, 54
Holoien T. W. S. et al., 2014, MNRAS, 445, 3263
Holoien T. W.-S. et al., 2019, ApJ, 883, 111
Holoien T. W.-S. et al., 2020, ApJ, 898, 161
Hung T. et al., 2019, ApJ, 879, 119
Inserra C., Prajs S., Gutierrez C. P., Angus C., Smith M., Sullivan M., 2018, ApJ, 854, 175
Ivezić Z. et al., 2019, ApJ, 873, 111
Jerkstrand A., Maeda K., Kawabata K. S., 2020, Science, 367, 415
Jiang N., Wang T., Hu X., Sun L., Dou L., Xiao L., 2021, ApJ, 911, 31
Jiang N., Zhou Z., Zhu J., Wang Y., Wang T., 2023, ApJ, 953, L12
Kennicutt R. C., Jr, Tamblyn P., Congdon C. E., 1994, ApJ, 435, 22

Kim S. S., Park M.-G., Lee H. M., 1999, ApJ, 519, 647
Kochanek C. S. et al., 2017, PASP, 129, 104502
Kumar H. et al., 2024, ApJ, 974, L36
Larson S., Brownlee J., Hergenrother C., Spahr T., 1998, BAAS, 30, 1037
Larson S., Beshore E., Hill R., Christensen E., McLean D., Kolar S., McNaught R., Garradd G., 2003, BAAS, 35, 982
Leloudas G. et al., 2016, Nat. Astron., 1, 1
Leloudas G. et al., 2019, ApJ, 887, 218
Mahabal A. A. et al., 2011, Bull. Astron. Soc. India, 39, 387
Mainzer A. et al., 2014, ApJ, 792, 30
Margutti R. et al., 2019, ApJ, 872, 18
Masci F. J. et al., 2019, PASP, 131, 018003
Masterson M. et al., 2024, ApJ, 961, 211
Matsumoto T., Piran T., 2021, MNRAS, 502, 3385
Metzger B. D., 2022a, ApJ, 932, 84
Metzger B. D., 2022b, ApJ, 937, L12
Meynet G., Maeder A., 2003, A&A, 404, 975
Miller A. A. et al., 2025, PASP, 137, 094204
Mockler B., Guillochon J., Ramirez-Ruiz E., 2019, ApJ, 872, 151
Mullaney J. R., Ward M. J., 2008, MNRAS, 385, 53
Mummery A., Balbus S. A., 2020, MNRAS, 497, L13
Mummery A., van Velzen S., Nathan E., Ingram A., Hammerstein E., Fraser-Taliente L., Balbus S., 2024, MNRAS, 527, 2452
Nakar E., Sari R., 2010, ApJ, 725, 904
Nicholl M. et al., 2023, ApJ, 954, L28
Nishiyama S., Schödel R., 2013, A&A, 549, A57
Nordin J., Brinnel V., Giomi M., Santen J. V., Gal-yam A., Yaron O., Schulze S., 2019, Transient Name Server Discovery Report, 2019-464, 1
O'Connor B. et al., 2025, ApJ, 979, L30
Oates S. R. et al., 2024, MNRAS, 530, 1688
Ofek E. O. et al., 2007, ApJ, 659, L13
Oke J. B., Gunn J. E., 1982, PASP, 94, 586
Oke J. B. et al., 1995, PASP, 107, 375
Pak M., Lee J. H., Jeong H., Jeong W.-S., 2023, AJ, 165, 109
Parkinson E. J., Knigge C., Matthews J. H., Long K. S., Higginbottom N., Sim S. A., Mangham S. W., 2022, MNRAS, 510, 5426
Pastorello A. et al., 2010, ApJ, 724, L16
Perley D. A. et al., 2019, MNRAS, 484, 1031
Perley D. A. et al., 2020, ApJ, 904, 35
Perley R. A., Chandler C. J., Butler B. J., Wrobel J. M., 2011, ApJ, 739, L1
Phinney E. S., 1989, Proc. IAU Symp. 136, The Center of the Galaxy. Kluwer Academic Publishers, Dordrecht, p. 543
Prieto J. L. et al., 2014, Astron. Telegram, 5831, 1
Rees M. J., 1988, Nature, 333, 523
Rehemtulla N. et al., 2024, ApJ, 972, 7
Reusch S. et al., 2022, Phys. Rev. Lett., 128, 221101
Reynolds T. M., Mattila S., Efstathiou A., Kankare E., Kool E., Ryder S., Peña Moñino L., Pérez-Torres M. A., 2022, A&A, 664, A158
Rigault M. et al., 2019, A&A, 627, A115
Rodrigo C., Solano E., 2020, Contributions to the XIV.0 Scientific Meeting (virtual) of the Spanish Astronomical Society, 182
Rodrigo C., Solano E., Bayo A., 2012, SVO Filter Profile Service Version 1.0, IVOA Working Draft
Roming P. W. A. et al., 2005, Space Sci. Rev., 120, 95
Ryu T., Krolik J., Piran T., 2020, ApJ, 904, 73
Sarin N., Metzger B. D., 2024, ApJ, 961, L19
Sarin N. et al., 2024, MNRAS, 531, 1203
Sazonov S. et al., 2021, MNRAS, 508, 3820
Schlafly E. F., Finkbeiner D. P., 2011, ApJ, 737, 103
Shappee B. J. et al., 2014, ApJ, 788, 48
Shen R.-F., Barniol Duran R., Nakar E., Piran T., 2015, MNRAS, 447, L60
Shen X., Hopkins P. F., Faucher-Giguère C.-A., Alexander D. M., Richards G. T., Ross N. P., Hickox R. C., 2020, MNRAS, 495, 3252
Shingles L. et al., 2021, Transient Name Server AstroNote, 7, 1
Smith K. W. et al., 2020, PASP, 132, 085002
Smith N. et al., 2007, ApJ, 666, 1116
Speagle J. S., 2020, MNRAS, 493, 3132

Steeghs D. et al., 2022, MNRAS, 511, 2405

Stein R. et al., 2021, Nat. Astron., 5, 510

Stickel M., Padovani P., Urry C. M., Fried J. W., Kuehr H., 1991, ApJ, 374, 431

Stone N., Sari R., Loeb A., 2013, MNRAS, 435, 1809

Subrayan B. M. et al., 2023, ApJ, 948, L19

Sukhbold T., Woosley S. E., 2016, ApJ, 820, L38

Team T. C., 2022, PASP, 134, 114501

Thompson A. R., Clark B. G., Wade C. M., Napier P. J., 1980, ApJS, 44, 151

Tonry J. L. et al., 2018, PASP, 130, 064505

Trakhtenbrot B. et al., 2019, Nat. Astron., 3, 242

Urry C. M., Scarpa R., O'Dowd M., Falomo R., Pesce J. E., Treves A., 2000, ApJ, 532, 816

Vanden Berk D. E. et al., 2001, AJ, 122, 549

van Velzen S. et al., 2019, ApJ, 872, 198

van Velzen S. et al., 2021, ApJ, 908, 4

van Velzen S. et al., 2024, MNRAS, 529, 2559

Vinkó J. et al., 2014, ApJ, 798, 12

Virtanen P. et al., 2020, Nat. Methods, 17, 261

van der Walt S., Crellin-Quick A., Bloom J., 2019, J. Open Source Softw., 4, 1247

Wevers T. et al., 2019, MNRAS, 488, 4816

Wiseman P. et al., 2023, MNRAS, 522, 3992

Wiseman P. et al., 2025, MNRAS, 537, 2024

Wright E. L. et al., 2010, AJ, 140, 1868

Yan L. et al., 2019, ApJ, 874, 44

Yao Y. et al., 2022, ApJ, 937, 8

Yao Y. et al., 2023, ApJ, 955, L6

Yao Y., Lu W., Harrison F., Kulkarni S. R., Gezari S., Guolo M., Cenko S. B., Ho A. Y. Q., 2024, ApJ, 965, 39

Yao Y. et al., 2025, ApJ, 993, 198

Yuan C., Winter W., Lunardini C., 2024, ApJ, 969, 136

SUPPORTING INFORMATION

Supplementary data are available at *MNRAS* online.

AT2018jbv_paperphotometry.csv
AT2019cmw_paperphotometry.csv

Please note: Oxford University Press is not responsible for the content or functionality of any supporting materials supplied by the authors. Any queries (other than missing material) should be directed to the corresponding author for the article.

APPENDIX A: SUPPLEMENTARY DATA TABLES

Photometry of AT2019cmw, and supplementary LT photometry of AT2018jbv, are presented in Tables A1 and A2, respectively. Blackbody parameters derived using the methods described in Section 3.2 for AT2019cmw and AT2018jbv are presented in Tables A3 and A4.

Table A1. Optical/UV photometry of AT2019cmw. We list only the first ten entries of AT2019cmw's photometry here, the full data are available in the supplementary online content.

MJD	mag	magerr	band	instrument
58594.143710	18.709	0.099	g	LT
58598.226021	18.706	0.043	g	LT
58603.229402	18.731	0.048	g	LT
58603.101068	18.750	0.044	g	LT
58607.077287	18.781	0.039	g	LT
58608.207288	18.833	0.038	g	LT
58611.058513	18.805	0.036	g	LT
58613.151103	18.858	0.036	g	LT
58615.073996	18.930	0.039	g	LT
58617.212955	18.992	0.038	g	LT

Table A2. Supplementary LT photometry of AT2018jbv. We list only the first ten entries of AT2018jbv's photometry here, the full data are available in the supplementary online content.

MJD	mag	mag err	band	telescope
58547.047175	19.332	0.073	g	LT
58566.029862	19.293	0.167	g	LT
58584.987308	19.509	0.074	g	LT
58595.002000	19.484	0.124	g	LT
58879.239850	20.749	0.095	g	LT
58896.150785	20.863	0.079	g	LT
58925.070166	20.932	0.080	g	LT
58959.973530	21.126	0.086	g	LT
58985.930979	21.070	0.082	g	LT
59024.922616	21.092	0.091	g	LT

Table A3. Blackbody characteristics of AT2019cmw derived using the methods described in Section 3.2.

Phase Days from peak (rest frame)	Temperature log(T/K)	Temperature error log(T/K)	Radius log(R/cm)	Radius error log(R/cm)	Luminosity log(L/ergs^{-1})	Luminosity error log(L/ergs^{-1})
−21.659	4.451	0.047	14.990	0.030	44.639	0.116
−20.342	4.451	0.047	15.130	0.020	44.918	0.100
−15.076	4.451	0.047	15.363	0.007	45.382	0.095
−14.417	4.451	0.047	15.367	0.011	45.393	0.096
−11.784	4.451	0.047	15.413	0.006	45.483	0.095
−3.884	4.451	0.047	15.471	0.003	45.599	0.094
−2.567	4.451	0.047	15.473	0.006	45.605	0.095
−1.909	4.451	0.047	15.475	0.002	45.608	0.094
4.674	4.441	0.039	15.466	0.036	45.550	0.171
7.966	4.463	0.045	15.434	0.040	45.572	0.198
10.599	4.478	0.020	15.413	0.021	45.590	0.091
13.232	4.514	0.054	15.375	0.046	45.659	0.234
14.549	4.284	0.010	15.594	0.016	45.175	0.050
15.866	4.439	0.038	15.427	0.036	45.461	0.169
20.474	4.251	0.037	15.646	0.091	45.151	0.233
22.449	4.300	0.055	15.547	0.061	45.148	0.254
23.766	4.277	0.009	15.561	0.013	45.082	0.046
26.399	4.354	0.019	15.462	0.024	45.192	0.091
44.832	4.166	0.044	15.573	0.058	44.661	0.212
52.074	4.171	0.027	15.561	0.036	44.659	0.130
63.265	4.182	0.013	15.501	0.021	44.584	0.067
98.157	4.052	0.029	15.634	0.050	44.332	0.153
115.932	4.131	0.065	15.502	0.100	44.382	0.326
146.215	4.047	0.023	15.570	0.040	44.179	0.121
203.489	3.930	0.045	15.704	0.093	43.982	0.260
210.072	3.986	0.029	15.564	0.055	43.927	0.159
229.164	4.017	0.041	15.447	0.082	43.814	0.232
242.989	3.891	0.054	15.707	0.118	43.832	0.319
296.313	3.836	0.057	15.704	0.130	43.604	0.345

Table A4. Blackbody characteristics of AT2018jbv derived using the methods described in Section 3.2. The phase of each fitted epoch is set according to the peak time of MJD 58469.19 for AT2018jbv from E. Hammerstein et al. (2023).

Phase days from peak (rest frame)	Temperature log(T/K)	Temperature Error log(T/K)	Radius log(R/cm)	Radius Error log(R/cm)	Luminosity log(L/ergs^{-1})	Luminosity Error log(L/ergs^{-1})
53.590	4.463	0.028	15.210	0.041	45.123	0.141
58.067	4.452	0.083	15.158	0.071	44.977	0.359
68.515	4.425	0.029	15.229	0.043	45.012	0.145
72.246	4.274	0.133	15.346	0.130	44.640	0.593
78.963	4.398	0.037	15.228	0.060	44.902	0.191
84.187	4.397	0.037	15.232	0.060	44.905	0.191
85.679	4.414	0.102	15.152	0.089	44.811	0.444
89.410	4.338	0.031	15.333	0.053	44.872	0.163
93.888	4.424	0.138	15.152	0.112	44.854	0.596
94.634	4.596	0.104	14.972	0.087	45.180	0.450
114.784	4.219	0.303	15.336	0.194	44.400	1.273
158.813	4.325	0.039	15.214	0.067	44.581	0.207
305.828	4.557	0.207	14.785	0.129	44.652	0.866
318.515	4.465	0.132	14.844	0.103	44.399	0.567
340.157	4.347	0.100	14.944	0.092	44.127	0.439
365.530	4.333	0.124	14.919	0.116	44.022	0.548
384.933	4.498	0.263	14.788	0.158	44.423	1.097
414.037	4.540	0.219	14.729	0.129	44.469	0.912

APPENDIX B: COOLING ENVELOPE MODEL POSTERIOR DISTRIBUTIONS

Fig. B1 shows the full posterior distribution inferred by our cooling envelope model fit to AT2019cmw's multiband photometry, as detailed in Section 5.1. Fig. B2 also shows the full posterior distribution inferred by our fit to our derived bolometric luminosities for AT2019cmw from Section 3.2, as detailed in Section 5.3.
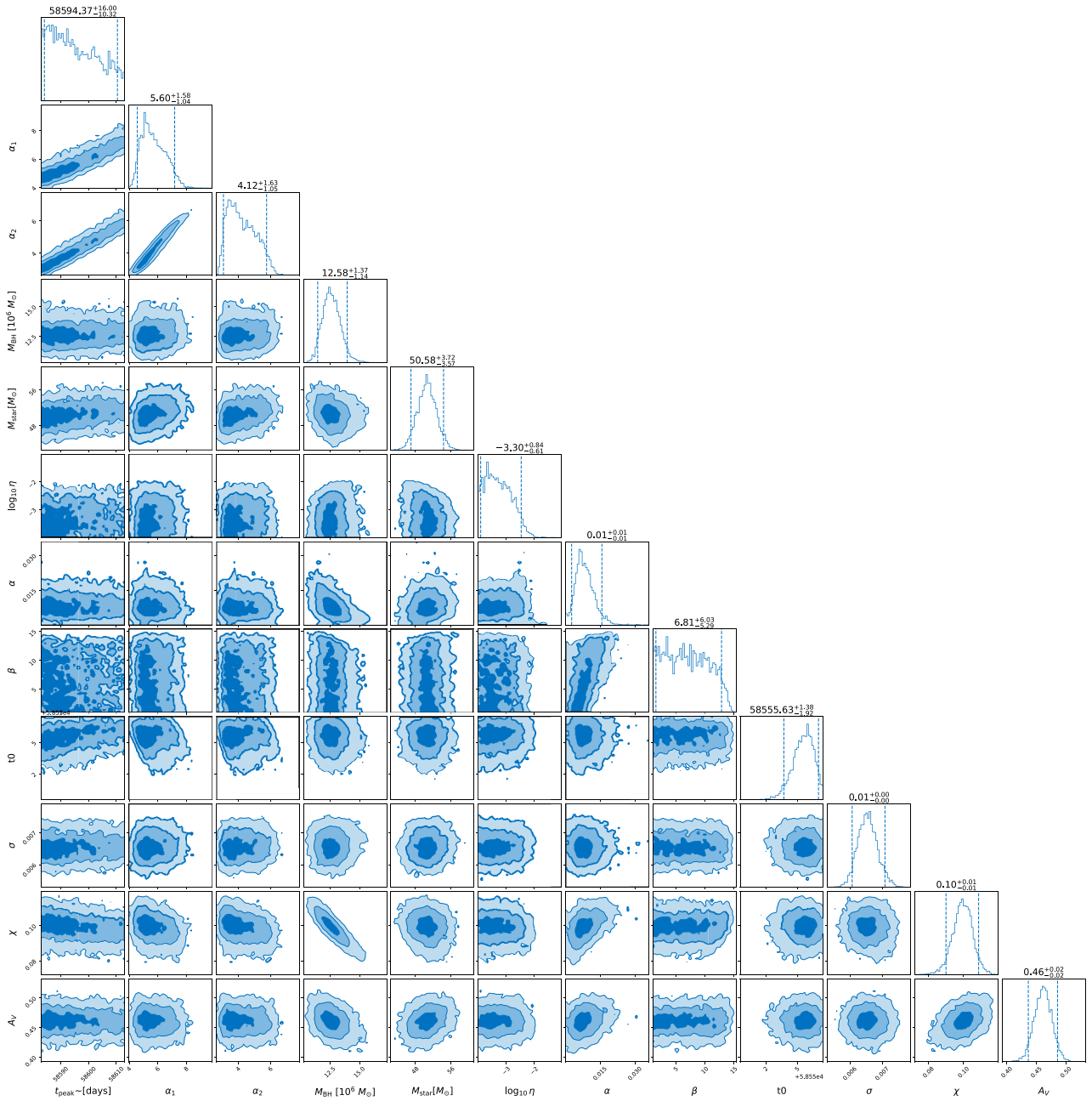
Figure B1. Inferred parameters from our model fit detailed in Section 5.1. Plot made using CORNER (D. Foreman-Mackey 2016).
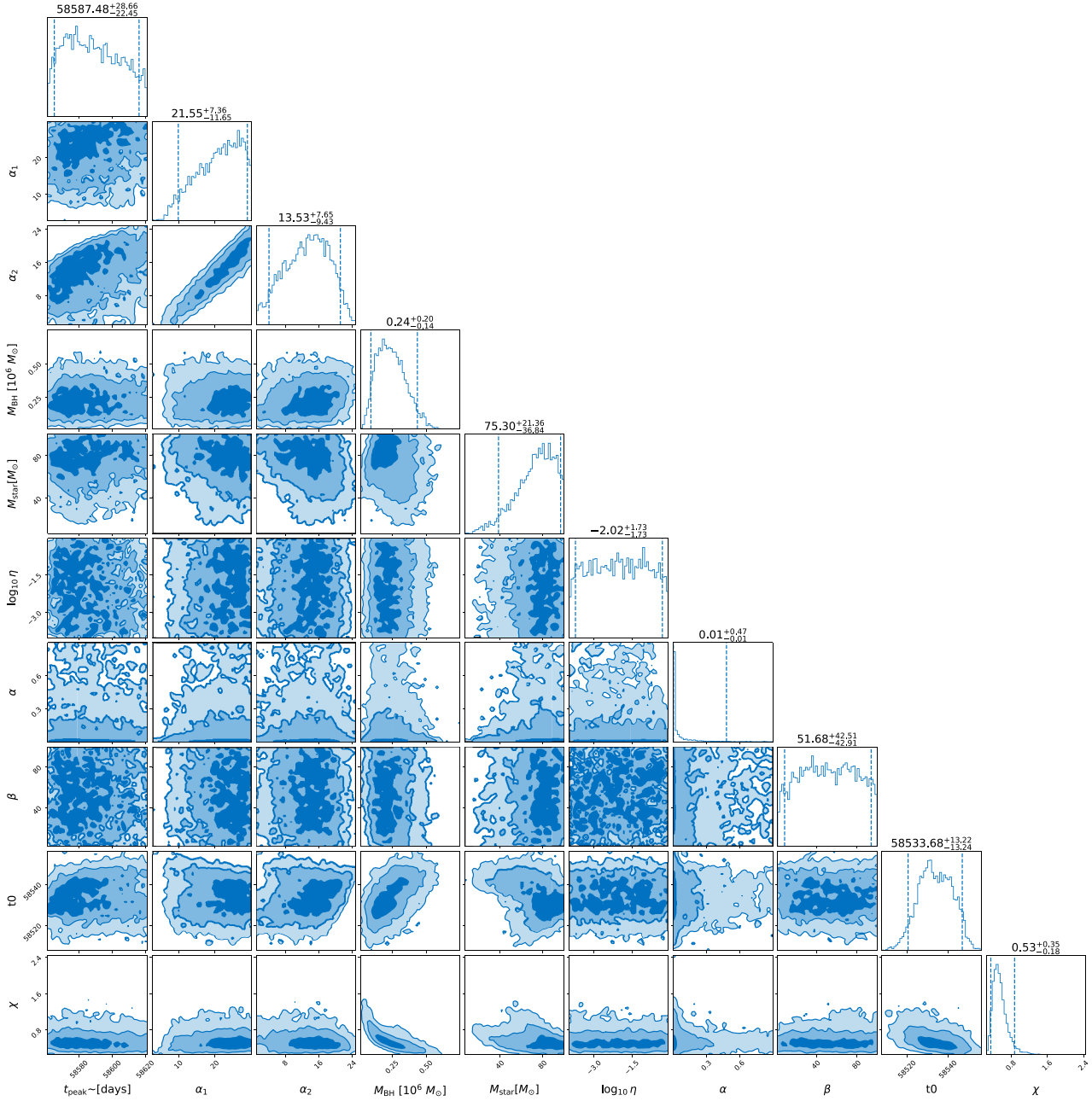
Figure B2. Inferred parameters from our model fit detailed in Section 5.3. Plot made using CORNER (D. Foreman-Mackey 2016).

APPENDIX C: COOLING ENVELOPE MODEL PREDICTED CHARACTERISTICS

Figs C1 and C2 show the photospheric blackbody characteristics predicted by our cooling envelope model fits from Sections 5.1 and 5.3, respectively. We also present proxy X-ray luminosities predicted by our model fit from Section 5.1 in Fig. C3.
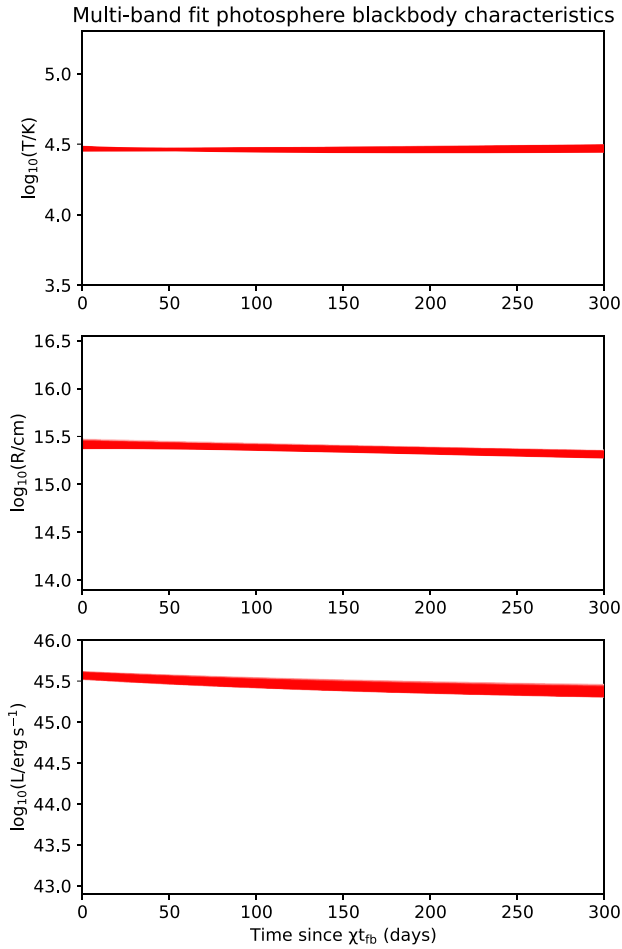

Figure C1. Photospheric blackbody temperatures (**top**), radii (**middle**), and luminosities (**bottom**) predicted for AT2019cmw by our model fit from Section 5.1 up to 300 d post-envelope formation.
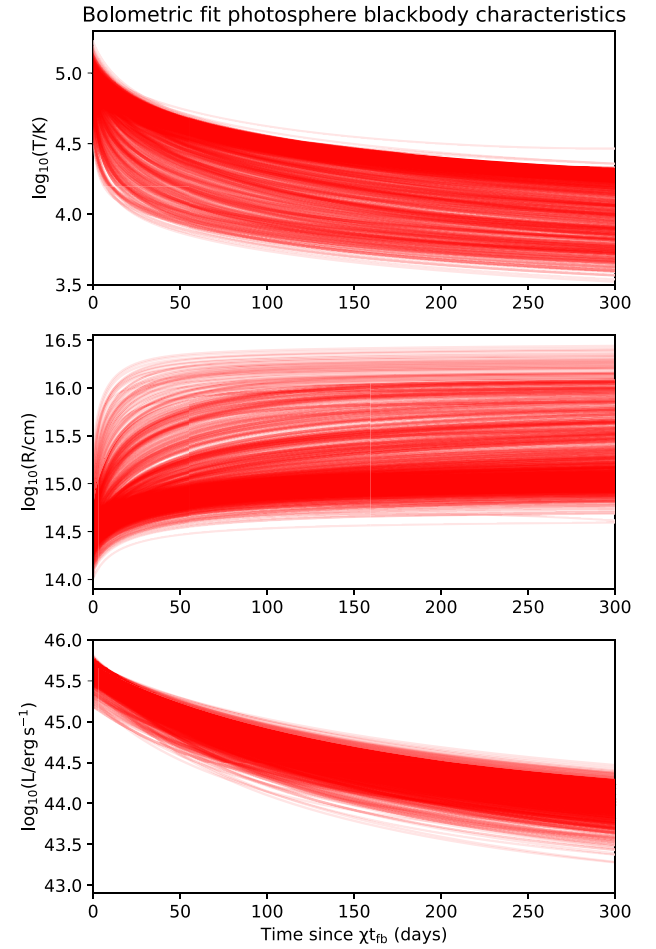

Figure C2. Photospheric blackbody temperatures (**top**), radii (**middle**) and luminosities (**bottom**) predicted for AT2019cmw by our model fit from Section 5.3 up to 300 d post-envelope formation.
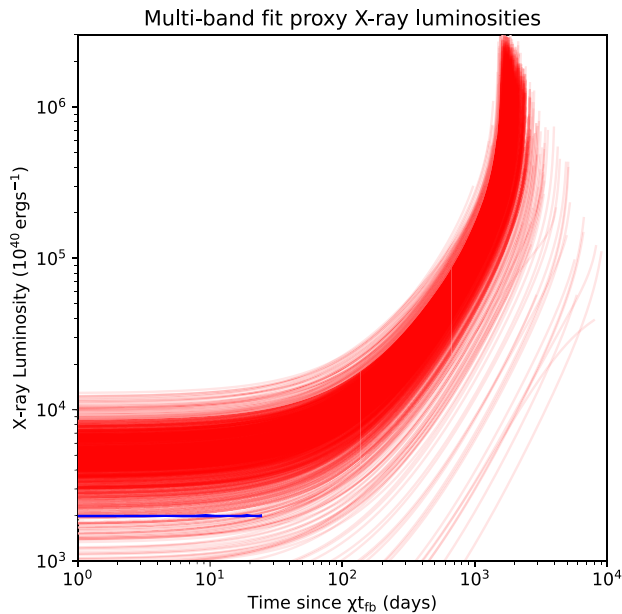
Figure C3. Proxy X-ray luminosities predicted for AT2019cmw by our model fit from Section 5.1 up to 10^4 d post-envelope formation, shown in red. Our upper limit on AT2019cmw's X-ray luminosity from Section 3.5 is shown as a blue horizontal line.

[1] *Astrophysics Research Institute, Liverpool John Moores University, 146 Brownlow Hill, Liverpool L3 5RF, UK*

[2] *Oskar Klein Centre for Cosmoparticle Physics, Department of Physics, Stockholm University, AlbaNova, Stockholm SE-106 91, Sweden*

[3] *Department of Astronomy, Kyoto University, Kitashirakawa-Oiwake-cho, Sakyo-ku, Kyoto, 606-8502, Japan*

[4] *Hakubi Center, Kyoto University, Yoshida-honmachi, Sakyo-ku, Kyoto, 606-8501, Japan*

[5] *Department of Astronomy, School of Science, the University of Tokyo, Bunkyo-ku, Tokyo 113-0033, Japan*

[6] *Miller Institute for Basic Research in Science, 206B Stanley Hall, Berkeley, CA 94720, USA*

[7] *Department of Astronomy, University of California, Berkeley, CA 94720-3411, USA*

[8] *Oskar Klein Centre, Department of Astronomy, Stockholm University, AlbaNova, SE-106 91 Stockholm, Sweden*

[9] *Center for Interdisciplinary Exploration and Research in Astrophysics (CIERA), Northwestern University, 1800 Sherman Road, Evanston, IL60201, USA*

[10] *School of Physics and Astronomy, University of Minnesota, Minneapolis, MN 55455, USA*

[11] *MIT Kavli Institute for Astrophysics and Space Research, 70 Vassar St., Cambridge, MA 02139, USA*

[12] *Caltech Optical Observatories, California Institute of Technology, Pasadena, CA 91125, USA*

[13] *Vanderbilt Department of Physics and Astronomy, 1221 Stevenson Center Lane, Nashville, TN 37240*

[14] *Division of Physics, Mathematics and Astronomy, California Institute of Technology, Pasadena, CA 91125, USA*

[15] *Space Telescope Science Institute, 3700 San Martin Dr, Baltimore, MD 21218, USA*

[16] *Physics and Astronomy Department, Johns Hopkins University, Baltimore, MD 21218, USA*

[17] *Cahill Center for Astrophysics, California Institute of Technology, MC 249-17, 1200 E California Boulevard, Pasadena, CA 91125, USA*

[18] *Department of Astronomy, Cornell University, Ithaca, NY 14853, USA*

[19] *IPAC, California Institute of Technology, 1200 E. California Blvd, Pasadena, CA 91125, USA*

[20] *Department of Physics, Drexel University, Philadelphia, PA 19104, USA*

[21] *Department of Astronomy and Astrophysics, University of California, Santa Cruz, CA 95064, USA*

[22] *Department of Astrophysical Sciences, Princeton University, Princeton, NJ 08544, USA*

This paper has been typeset from a TeX/LaTeX file prepared by the author.